Review

Superhydrophobic materials used for anti-icing Theory, application, and development

Hua He[1,2] and Zhiguang Guo[1,2,*]

SUMMARY

The accumulation of ice will reduce the performance of the base material and lead to all kinds of damage, even a threat to people's life safety. Recent increasing studies suggest that superhydrophobic surfaces (SHSs) originating from nature can remove impacting and condensing droplets from the surface before freezing to subzero temperatures, and it can be seen that hydrophobic/SH coating has good freezing cold resistance. But such anti-icing performances and developments in practical applications are restricted by various factors. In this paper, the mechanism and process of surface icing phenomenon are introduced, as well as how to prevent surface icing on SHS. The development of SH materials in the aspect of anti-icing in recent years is described, and the existing problems in the aspect of anti-icing are analyzed, hoping to provide new research ideas and methods for the research of anti-icing materials.

INTRODUCTION

In the nature, it is well known that surface icing and frosting are very common phenomena. It sometimes presents us with a kind of visual beauty, such as the unique phenomenon of sprinkling water becoming ice around Mohe River in northeast China. The sight is that when hot water is sprayed quickly into the air it forms a beautiful arc. In fact, it is because the temperature is so low that when pouring hot water into the air, a lot of water vapor condenses directly into ice crystals when it gets cold. In addition, the direct condensation of water vapor is also related to the local air particles and sufficient contact with the air. When the hot water poured out is sufficiently dispersed and fully exposed to the air, it will turn into a fog-like form. And these are interspersed with tiny ice crystals. Thus, the magical scene of water into ice appears. In addition, the ice may cause damage to road traffic, power transmission, building roofs, aircraft wings, wind turbines, ships, and other equipment surfaces, which impedes the operation of equipment, reduces the use efficiency of equipment and facilities, and even causes huge safety hazards (Azimi Yancheshme et al., 2020; Guo et al., 2020; Latthe et al., 2019; Wei et al., 2019; Yin et al., 2020).Every year, a large number of safety accidents are caused by surface icing, which not only threatens people's life safety but also causes huge economic losses. For instance, the road problems caused by rain and snow lead to greatly weakened wheel and road friction, which makes the vehicle out of control and results in traffic accidents. The ice on the pavement also makes it easy for pedestrians to slip and fall (Latthe et al., 2019). In addition, in 2008, there was a sudden snowfall in the South (in fact, freezing rain meets cooler objects and freezes quickly), the frost accumulation increased the weight of the wire. Many pylons were destroyed, which caused an economic loss of more than 16 billion dollars (Azimi Yancheshme et al., 2020; Guo et al., 2020; Latthe et al., 2019; Pan et al., 2020; Wei et al., 2019; Yin et al., 2020). And when the ice is formed on the equipment surface, it can not only increase the energy loss but also cause damage to the surface of the equipment.

The accumulation of ice on the wings of the plane can slow down the plane's flight speed and even lead to seriously reduced upward force. The increased weight of the aircraft will block the moving parts, resulting in the plane to crash (Latthe et al., 2019). Due to the ice on surface and increasing load and stress as well as vibration and turbulence, it inhibits the best performance of wind turbines and results in wind power equipment shutdown (Azimi Yancheshme et al., 2020). Large amounts of snow, ice, and supercooled water freezing on the surface of the hull change the center of gravity of vessels and reduce its stability, thus heightening the possibility of capsizing in Arctic shipping lanes (Azimi Yancheshme et al., 2020). For another example, in the low temperature environment, microelectronic materials (such as polymer sealant and chip connection film layer) may condense water vapor absorbed from the surrounding humid

[1]Ministry of Education Key Laboratory for the Green Preparation and Application of Functional Materials, Hubei University, Wuhan 430000, People's Republic of China

[2]State Key Laboratory of Solid Lubrication, Lanzhou Institute of Chemical Physics, Chinese Academy of Sciences, Lanzhou 730000, People's Republic of China

*Correspondence: zguo@licp.cas.cn

https://doi.org/10.1016/j.isci.2021.103357

environment into dew or even frost during transportation and storage, which will cause damage to the electronic equipment (Azimi Yancheshme et al., 2020). Icing usually affects the surface roughness of wind turbine blades and thus changes their aerodynamic performance. Moreover, it increases the total weight and load of the blades, causing a large amount of power loss and even the stopping of wind turbines due to the intervention of ice. In addition, uneven ice formation can lead to unstable blades, which can cause excessive vibration and damage to wind turbines, leading to safety problems and so on (Wei et al., 2019). Therefore, in the past few decades, scientists have conducted many studies to improve the deicing function performance on the surface, which can be roughly divided into two kinds of main strategy against freezing, active and passive methods.

Active method is mainly through external energy de-icing. There are many such methods and here is a simple introduction of several. For example, the principle of electric heating anti-icing is through applying an electric current by the electric heating element, melting the ice, and reducing the binding force between the ice and the surface (Ibrahim et al., 2019; Pan et al., 2020). Especially, heating the wire is an effective method to remove the icing on the transmission line. However, there is a large energy loss and cost, and this method harnesses the current, which may cause electromagnetic interference to the equipment (Lv et al., 2014). Hot air anti-icing is commonly used in the anti-icing system of aircraft. The principle is that electric energy is converted into heat energy by heating resistance, and the heated hot air flow is sent to the designated position to melt the ice attached on its surface. But this method is energy intensive and can cause damage to some materials on the plane. In serious cases, the equipment on the plane may malfunction, causing the plane to crash. Liquid anti-icing, is also known as chemical solution anti-icing. This method is to spray antifreeze liquid such as ethylene glycol, calcium chloride, and urea on the surface of the material (Talalay et al., 2019), which can reduce the freezing point of water or make ice melt easily. In winter, salt is often applied to remove the ice and snow on the road. Because of high solubility in sodium chloride (NaCl), 75%–90% of added salt is reported to enter roadside environment through runoff or splash. Ground water may be contaminated by salt solution percolation. In addition, roadside vegetations, as well as water creatures living alongside the roads, are seriously affected (Lv et al., 2014). Furthermore, certain chemical solutions are corrosive to metals (Ramakrishna, 2005). The ice on the surface of a material is mechanically broken and removed, which is defined as mechanical de-icing. It is mainly driven by directly hitting the ice or using other means such as pneumatic or electric power to drive the machine. This method is usually used for removing ice from equipments that are easily approached, such as overhead transmission lines and power networks. This method often requires that people get direct contact with the lines and high towers. Hence, there is a big security risk. During de-icing, mechanical forces put extra pressure on the network and in some cases can lead to failures (Lv et al., 2014).

However, these methods are complicated in design and have the disadvantages such as high energy consumption, high application cost, and time consuming. Therefore, it is of great significance to study effective anti-icing methods. Passive methods, as a strategy to improve active methods, refer to the physical and chemical methods based on surface modification (Cho et al., 2015). With advances in nanotechnology and bionics, SH materials are considered a suitable anti-icing material due to their special surface structure. It is hoped that they can better replace traditional active methods in ideal application conditions without consuming any other energy.

Typically, researchers place droplets on a solid surface with a water contact angle (WCA) greater than 150° and a sliding angle (SA) less than 5°, known as an SHS. The initial inspiration of SHS comes from the lotus leaf effect. German botanists Barthlott and Neinhuis (Barthlott and Neinhuis, 1997) revealed the surface structure of lotus leaves and found that the self-cleaning effect of lotus leaves is due to the micro-nano structure of its surface. There are micron papillae on the surface of the lotus leaf, and the papillae are covered with a thin layer of nano-waxy crystals, which can greatly improve the CA of water droplets on the surface of the lotus leaf and make the water droplets fall easily. Wang et al. (2009a) believed that another important reason for lotus leaf's SH effect was the nanoscale structure on the surface of mastoid process and waxy crystal. Some people have also observed the microscopic characteristics of the surface of the lotus leaf and found that the surface of the lotus leaf has a random distribution of nearly hemispherical papillae with the size of 5–10 μm and about 150 nm dendritic mastoid, as shown in the Figure 1A. And the surface of the lotus leaf showed almost completely suspended water droplets (Zorba et al., 2008). In general, the "lotus effect" refers to the self-cleaning ability of the surface of the lotus leaf. When the water droplets fall on the lotus leaf, because the SA of the water on SHS is very small, the water droplets cannot
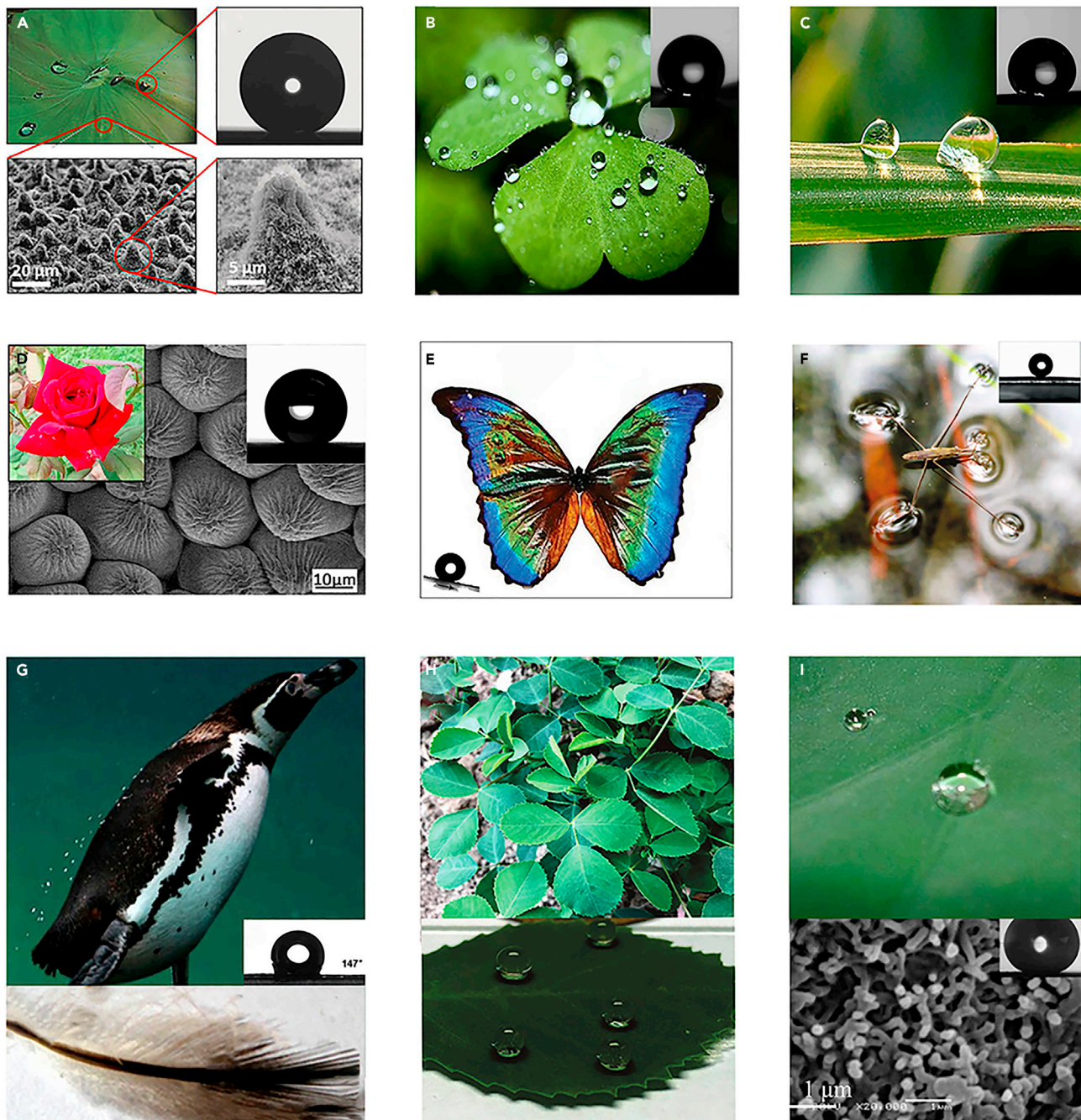
Figure 1. SH plants and animals in nature

(A) Nature-inspired nanostructures for special nonwetting states. The lotus leaf surface and its microscopic features. Optical image of a droplet statically sitting on the surface of lotus leaf. Image reprinted with permission from Zorba et al. (2008).

(B) Water droplet beading on clover; (inset of (B)) a WCA of clover is 152°, showing a good SH property.

(C) Water droplet beading on green Bristlegrass; (inset of (C)) a water CA of green Bristlegrass is 153°, showing a good SH property. Image reprinted with permission from Liu et al. (2019a).

(D) ESEM images of a Chinese red rose petal with rich surface textures in microscale and shape of a water droplet on the petal's surface, indicating its hydrophobicity with a CA of 149.8°. Image reprinted with permission from Chen et al. (2018).

(E) An iridescent blue butterfly. Image reprinted with permission from Zheng et al. (2007).

stay on the surface of the lotus leaf. The spherical droplets mingled with the dust attach on the surface of the lotus leaf and tumble down, leaving a clean surface of the lotus leaf. In nature, many plants and animals have SHS similar to lotus leaf, such as rose petals (Bhushan and Her, 2010; Chen et al., 2018), clover (Liu et al., 2019a), taro leaves (Chen et al., 2017; Yi et al., 2019), water striders (Gao and Jiang, 2004; Lu et al., 2018), butterfly wings (Zheng et al., 2007), the penguin body feather (Wang et al., 2016), and so on (Figure 1). Inspired by different plants and insects, researchers have developed many SHSs. Currently, SHSs are used not only for self-cleaning (Jeevahan et al., 2018), oil/water separation (Lv et al., 2018), water collection (Tian and Wang, 2018), and anti-corrosion (Sebastian et al., 2018) but also for anti-icing and other applications (Si et al., 2018). It is found that the SH characteristics of solid surface mainly depend on its low surface energy and rough microstructure. Hence, the method to obtain the SH characteristics is to modify and fabricate rough micro surface structure with low surface energy materials on solid surface. In order to construct this SH structure, the researchers used a number of preparation methods, which can be broadly classified as top-down or bottom-up. The usual top-down approach refers to the preparation of highly controlled micro-nanostructures by engraving or machining, with the help of tools and lasers such as photolithography (Fromel et al., 2020), laser treatment (Li et al., 2019b), plasma treatment (Ryu et al., 2017), anodic oxidation (Saji, 2020), etc. And the bottom-up approach refers to a material addition process or self-assembly process in which complex surface is formed by adding smaller building blocks of materials by nano- or microfabrication such as sol-gel technology, electrostatic spinning, coating, deposition, and so on (Jeevahan et al., 2018; Sun and Guo, 2019; Zhang et al., 2020). In conclusion, a suitable roughness on the hydrophobic surface could be created using these techniques and using chemical modification with hydrophobic materials (Pan et al., 2019; Wang et al., 2020b), such as stearic acid, fluoroalkyl silane, lauric acid, polydimethylsiloxane, Teflon, and so on, in order to reduce the surface energies and produce an SHS (Liu et al., 2017; Wang and Guo, 2019). For example, Qing et al. (Qing et al., 2019) used an ingenious two-step method to fill the concave microstructure of sandpaper matrix with a layer of fluorinated inorganic/organic film. The combination of the micro-nano structure and the low surface energy given by fluorinated nanoparticles resulted in FTPSS (FAS-TiO$_2$/PDMS SH sandpaper surface) with CA of 160.6° and SA of 3.9°. FTPSS retains its hydrophobic properties under several chemical and mechanical stresses such as finger wiping, water pressure, hot water, tape peeling, and sandpaper abrasion. In addition, surface wettability can be controlled effectively by changing mesh size of sandpaper template. Moreover, the sandpaper showed good resistance to snow and ice after being worn for 50 times and was able to prevent snow and ice from adhering to the substrate (Qing et al., 2019). Feng et al. (Feng et al., 2018) first prepared a layered SH aluminum alloy surface by one-step impregnation process and then grafted long hydrophobic alkyl chain stearic acid (STA) on the surface, so that a large amount of air was trapped on the surface. The SH aluminum alloy obtained by this method not only has rough surface but also has two kinds of compound structures in micron and nanometre scale.

When water droplets are applied to the surface, the contact area between water droplets and air is measured to account for about 92.0% of the total area. Compared with the blank aluminum alloy surface, the freezing time of the SH aluminum alloy surface can be delayed by 5–9 min, and the freezing temperature can be reduced to 2–4°C. It can be seen that the SHS has a certain anti-icing property (Feng et al., 2018).

In order to understand the suitability of SH materials in anti-icing, it is necessary to understand the formation process of ice and the corresponding methods to inhibit the formation and growth of ice, which is of great significance for the research of new anti-icing methods on solid surface and the improvement of the application of SH materials in anti-icing. The main content of this paper is the latest progress in the research of SH material for anti-icing. The formation process of ice on the material surface and the common strategies of SH material for anti-icing are summarized. Firstly, the mechanism of surface icing and the existence of critical ice core are summarized and discussed. Then it introduces the main characteristics of SH material for anti-icing, which is mainly divided into three parts. The first part is about being able to clean up surface
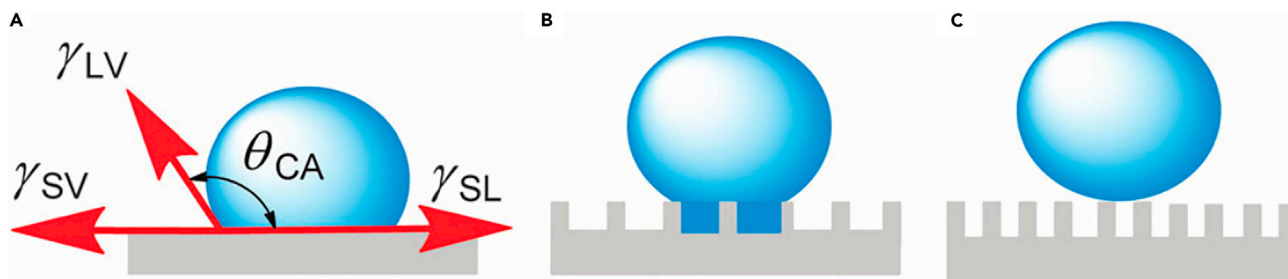
Figure 2. Schematic illustration of theoretical wetting models
Schematic illustration of a droplet placed onto a flat substrate (A) and rough substrates (B) and (C). Depending on the roughness of the surface, the droplet is either in the so-called Wenzel regime (B) or in the Cassie–Baxter (C) regime. Image reprinted with permission from Chu and Seeger (2014).

water droplets in time before freezing, especially the water droplets that collide on the surface and those that condense on the surface. The second part is about controlling the formation of ice cores on the surface after freezing, thus prolonging the freezing time. The third part is about reducing ice adhesion and facilitating the removal of ice. Then the practical application of some SH materials in anti-icing is briefly introduced, and some existing problems, such as the mechanical stability of SH materials, are introduced, and then some existing solutions are introduced. Finally, the conclusions and prospects of developing new anti-icing methods on solid surfaces and improving the application of SH materials in anti-icing are described.

Theoretical basis

Static contact angle

Young's equation. In 1805, Thomas Young proposed that when the solid, liquid, and gas phases reach equilibrium on an absolutely smooth and homogeneous ideal surface (Figure 2A), the θ_0 of the drop is related to the interfacial energies acting between the solid–liquid (γ_{SL}), solid–vapour (γ_{SV}), and liquid–vapour (γ_{LV}) interfaces (Chu and Seeger, 2014):

$$cos\theta_0 = \frac{\gamma_{SL} - \gamma_{SV}}{\gamma_{LV}} \qquad \text{(Equation 1)}$$

Young's equation only represents an ideal surface, and it only applies to the surface with uniform chemical composition and absolute smoothness. However, in reality, solid surface has uneven chemical composition and certain roughness. Therefore, two different models, the so-called Wenzel state (Wenzel, 2002) (Figure 2B) and Cassie–Baxter state (Cassie and Baxter, 1944) (Figure 2C), were developed to explain the wetting behavior on a rough surface (Chu and Seeger, 2014).

The Wenzel model. In 1936, Wenzel proposed the Wenzel model and modified the Young model by introducing roughness because the actual solid surface was not uniform and had some roughness. Wenzel model assumes that when liquid comes in contact with the rough solid surface, it can completely fill the grooves on the rough surface (as shown in Figure 2B). The contact between liquid and the surface of the surrounding body is in the mode of complete contact. Wenzel model can be expressed as follows:

$$cos\theta_1 = r\frac{\gamma_{SL} - \gamma_{SV}}{\gamma_{LV}} = rcos\theta_0 \qquad \text{(Equation 2)}$$

where θ_1 is the apparent CA of the rough surface, and r is defined as the roughness factor, which is the ratio of the actual area of the solid surface to the projected area. According to Wenzel model, for a specific surface, surface roughness has a magnifying effect on the wettability of solid surface: for the hydrophilic surface, the surface becomes more hydrophilic with the increase of surface roughness; for hydrophobic surfaces, surface roughness increases, and it leads to an increase in hydrophobicity. However, some hydrophilic materials can also produce SHSs through special treatment, which can not be explained by Wenzel theory, and Wenzel model is not applicable when the solid surface is composed of different chemical substances, indicating that Wenzel theory also has certain limitations (Chu and Seeger, 2014; Yu et al., 2015).

The Cassie-Baxter model. Cassie and Baxter envisioned the solid surface as a composite surface and assumed that when liquid came into contact with the rough surface, droplets of liquid could encase air

in the grooves of the composite surface, forming a solid-liquid-gas three-phase interface. In this case, the contact area of the water droplet consists of two parts, namely, the contact area between the water droplet and the solid surface, and the contact area between the water droplet and the gas trapped in the groove. In this way, Cassie model can be expressed as

$$cos\theta_2 = f_{SL}cos\theta_{SL} + f_{LV}cos\theta_{LV} \qquad \text{(Equation 3)}$$

where θ_2 is the apparent CA in the Cassie-Baxter state, f_{SL} and f_{LV} are respectively solid-liquid contact area fraction and gas-liquid contact area fraction ($f_{SL} + f_{LV} = 1$). θ_{SL} and θ_{LV} represent the CA of solid-liquid and gas-liquid, respectively.

When the liquid only touches the top of the solid convexity and the air pocket is stuck below the liquid, a polymorphic plane is formed between the solid and the air, as shown in Figure 1C. In such a polymorphic surface the air-dependent part of the surface can be considered to be in a nonhumid state. $\theta_{SL} = \theta_0$ and assuming that the CA between the air and the liquid, $\theta_{LV} = 180°$, Equation 3 can be converted to

$$cos\theta_2 = f_{SL}(cos\theta_0 + 1) - 1 \qquad \text{(Equation 4)}$$

According to Equation 4, when the air in the groove is completely filled with liquid, $f_{SL} = 1$, Cassie's equation is transformed into Wenzel's equation. At the same time, an SHS with large CA can be obtained by minimizing the contact fraction of solids (Li et al., 2021).
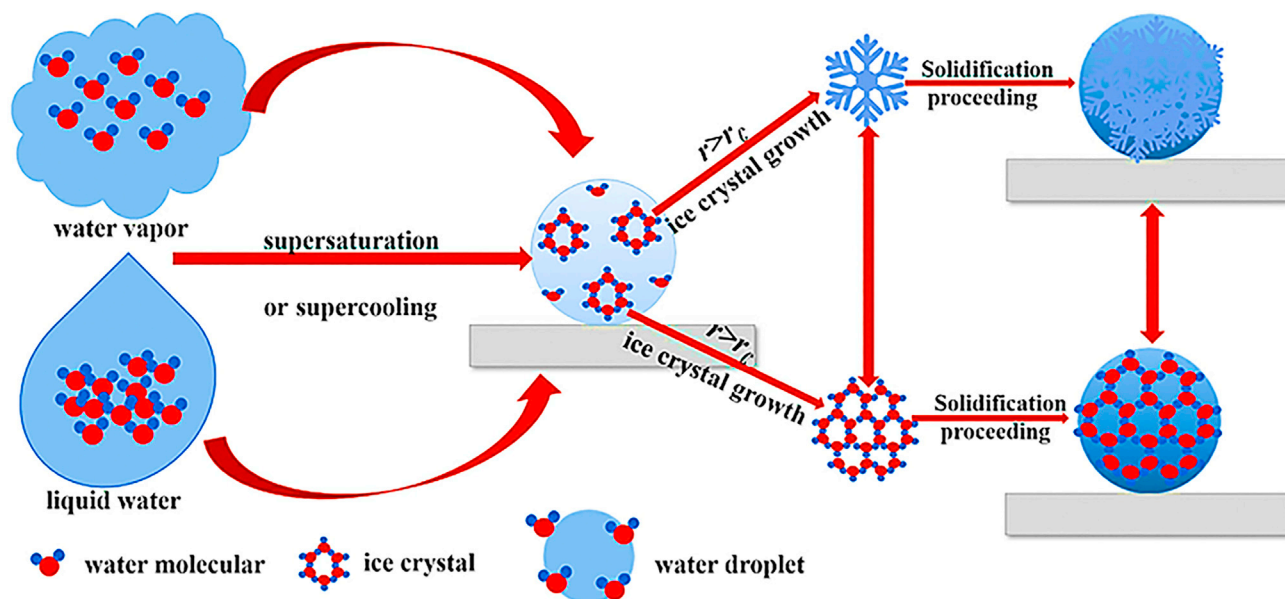
MECHANISM OF ICE FREEZING

In order to understand how SHSs are ice resistant, it is essential to understand the icing mechanism. Water freezing is a very common phenomenon in nature. In essence, the freezing of water droplets is a liquid-solid phase transition, which is triggered by nucleation of the new phase in water droplets and growth into three-dimensional ice crystals (Sear, 2007). Depending on the ambient temperature, atmospheric pressure, and formation process, the initial phase of the freezing process can be roughly divided into three types: ice crystals, supercooled water droplets, and ordinary water droplets. The first is solid hydrate in which water vapor grows on ice cores through a deposition process. The second is a water drop that exists as a liquid below freezing point (Lin et al., 2018). If the surface temperature is also below 0°C, it promotes the beginning of sparse dendritic crystal structures, also known as frost, nucleating from a vapor phase via condensation or sublimation. Taking into account the density of ice and surrounding temperature, three ice regimes can be recognized: glaze ice—transparent, rime ice—milky-white, and mixed ice (Esmeryan, 2020).

Just as water droplets on a solid surface turn into ice, under atmospheric conditions, the temperature of water must first drop below 0°C and become supercooled water. From the thermodynamic point of view, the ice phase is in a stable state. This transition process needs to use supersaturation and/or supercooling as driving forces to overcome the existing potential barrier (Li et al., 2021; Varanasi et al., 2009), as depicted in Figure 3. In the known research, ice formation is a complex phase transition phenomenon, and nucleation is the most basic and critical step in the process of water ice formation. During nucleation, the liquid water molecules with higher entropy will be transformed into crystalline solid ice with lower entropy (Li et al., 2021), and the initial embryo of the crystal will form in the supercooled/supersaturated parent phase. Whether the crystalline phase can form and the mass of the final crystal depends on the nucleation process to a great extent (Lin et al., 2018). Nucleation is a process of energy exchange, that is, the rapid exchange of heat at the solid-liquid interface after the supercooled droplet contacts the solid surface (Xie et al., 2019). When an ice nucleus reaches or exceeds the critical size in supercooled water, the freezing process begins, and the ice core grows in the supercooled water and eventually becomes ice in the macroscopic sense. The macroscopic formation and microscopic growth of ice cores are shown in Figure 3. At the same time, the formation of ice cores is a random phenomenon, that is, the probability distribution of the subcooling degree of water during the formation of ice cores is within a certain range. There are two mechanisms for the formation of ice nucleation: one is uniform nucleation in the water body, and the other is heterogeneous nucleation at the solid-liquid variable interface (it is also called heteronucleation). The following is a simple analysis of the two existing mechanisms.

HOMOGENEOUS NUCLEATION

Assuming that, under ideal conditions, the ice nucleation process is unaffected by impurity particles or the outer surface, the probability of forming a critical nucleus is uniform throughout the system, which is called homogeneous nucleation (as show in Figure 4B). Regarding a drop of water as a system, in a

Figure 3. Schematic diagram of mechanism of ice formation (r and r_c are the size radius and critical size radius of an embryo, respectively)
Image reprinted with permission from Li et al. (2021).

supercooled/supersaturated system, first of all, a certain range of water molecules is spontaneously bonded together by hydrogen bonds because of the thermodynamic driving force. Due to hydrogen bond interactions, more and more water molecules are connected to each other. By analyzing molecular dynamics simulations of water freezing, Shen et al. (2019a) showed that water molecules spontaneously join into many small rings at the junctions of hydrogen bonds. Subsequently, some individual rings are broken and continuously rearranged, with occasional random occurrences of more stable hydrogen bonds at different locations. With the extension of time, the polyhedral structure of the tiny crystal nucleus grows slowly. The droplets slowly changed in shape and size by constantly adjusting the hydrogen bonds around them and then developed toward a more stable state with a lower energy structure, allowing them to switch from liquid to solid. The formation of a new interface results in the decrease of the free energy of the system, and the accumulation of ice nucleus increases the free energy of the interface between ice nucleus and liquid water (Gohari et al., 2017; Li and Guo, 2018; Lin et al., 2018). Assuming that the crystal embryo formed is a sphere with a radius of r, the total change of free energy caused by phase transition can be expressed as the sum of the reduction of free energy of the volume crystal and the increase of free energy of the surface, namely

$$\Delta G_{Homo} = -\frac{4}{3}\pi r^3 \Delta G_v + 4\pi r^2 \sigma \qquad \text{(Equation 5)}$$

σ is the specific surface energy, expressed by the interfacial tension at ice-water interface, and ΔG is the free energy change of the system, which conforms to the Gibbs-Helmholtz equation:

$$\Delta G_v = \frac{\Delta H(T_m - T)}{T_m} \qquad \text{(Equation 6)}$$

Furthermore, $\Delta H = 287 MJ/m^3$ is the water volumetric enthalpy of fusion, and $T_m = 273K$ is the ice melting point under one bar, respectively (Li and Guo, 2018).

From the Figure 4A, under a certain temperature, when reaching maximum ΔG, $r = r_c$, where r_c is the critical nucleation radius, the r_c is the critical radius for short. The critical radius r_c can be obtained by calculating the extremum, assuming that $\frac{d\Delta G^*_{Homo}}{dr} = 0$. The results are represented by

$$r_c = -\frac{2\sigma}{\Delta G_v} \qquad \text{(Equation 7)}$$
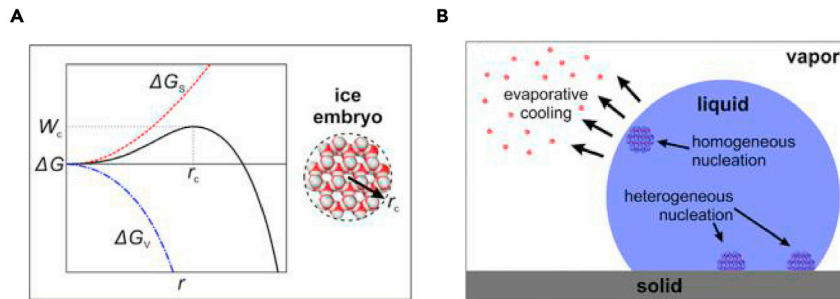
Figure 4. Schematics illustrating important aspects of nucleation

(A) Homogeneous nucleation. Plot of ΔG versus embryo radius (r), showing that beyond a critical value, r_c, the growth of the ice embryo is energetically favorable (homogeneous nucleation). The inset image is a schematic of an ice embryo of critical size.

(B) Nucleation. Schematic depicting the regions within a water droplet where ice can nucleate and potential influences (e.g., evaporation). Image reprinted with permission from Schutzius et al. (2015).

$$\Delta G^*_{Homo} = \frac{16\pi\sigma^3}{3\Delta G_v^2} \qquad \text{(Equation 8)}$$

ΔG^*_{Homo} is the so-called nucleation barrier.

When establishing Equations 6 and 7, r_c can be expressed as

$$r_c = -2\sigma T_m/[\Delta H(T_m - T)] \qquad \text{(Equation 9)}$$

This critical size varies with the varying degree of supercooling. The greater the subcooling degree, the smaller the critical radius r^*. In consequence, both the probability of ice nucleus formation and the number of ice nucleus increase.

It has been reported that SHSs delay the freezing time of ice on the surface, so it is necessary to discuss the nucleation rate. The uniform nucleation rate can be calculated by the following formula:

$$J_{Homo} = K \cdot N \cdot \exp\left(-\frac{\Delta G}{k_B T}\right) \qquad \text{(Equation 10)}$$

In this formula, K is the kinetic prefactor for the stable attraction between free water molecules transferred to ice embryo, N is the volume-based quantity density of water molecules in liquid parent phase, and k_B and T represent the Boltzmann constant and ambient temperature of the droplet, and $\Delta G = \Delta G^*_{Homo} + \Delta G_{act}$ is the sum of critical Gibbs free energy barrier and activation energy barrier. The ΔG^*_{Homo} is the main factor. The nucleation rate J increases with the decrease of temperature (Niu et al., 2019).

HETEROGENEOUS NUCLEATION

In most actual ice forming processes, the aforementioned homogeneous nucleation occurs very rarely. Nucleation is often promoted due to the presence of airborne contaminants and foreign matter on the walls of the container, such as foreign matter particles or substrates. In addition, the solid surface can also reduce the nucleation energy barrier. The presence of a foreign body usually reduces the free energy of the interface (or surface), thus reducing the nucleation barrier (Zhang and Liu, 2018). Therefore, nucleation occurs tremendously near or on foreign bodies, which is a process known as heteronucleation (as show in Figure 4B).

The icing process on a certain surface could be considered as a phase transition. The whole process would certainly be affected by the WCA. The phase transition causes the decrease of Gibbs free energy (Wang et al., 2019b). Because there are other things in the droplet, such as foreign bodies or nucleating agents, which reduce the critical thermodynamic nucleation barrier to accelerate the formation of the critical ice nucleus, the free energy barrier of heterogeneous nucleation is lower than that of uniform ice nucleation. The formula can well express the relationship between the two:

$$\Delta G^*_{Heter} = \Delta G^*_{Homo} fr, \theta \qquad \text{(Equation 11)}$$

$$fr, \theta = \frac{(2+\cos\theta)(1-\cos\theta)^2}{4} \qquad \text{(Equation 12)}$$

ΔG^*_{Heter} is the homogeneous nucleation barrier, and the parameter fr, θ is a function of the static CA (θ) for water droplet and surface roughness radius of curvature (r). The value of f varies from 0 to 1 (Wang and Guo, 2019). When the value of f is 1, the energy required for a completely nonwet surface ($\theta = 180°$) is equal to that of a uniform surface.

In addition, f can be replaced by another expression, which elaborates the specific meaning and application of r, $r*$, and m.

$$f(m,x) = \frac{1}{2} + \frac{1}{2}\left(\frac{1-mx}{\omega}\right)^3 + \frac{1}{2}x^3\left[2 - 3\left(\frac{x-m}{\omega}\right) + \left(\frac{x-m}{\omega}\right)^3\right] + \frac{3}{2}mx^2\left(\frac{x-m}{\omega} - 1\right) \qquad \text{(Equation 13)}$$

In this case, $x = r/r*$, $\omega = (1 + x^2 - 2xm)^{\frac{1}{2}}, m = \cos\theta$. ω is the CA at ice-water interface, and x denotes the effect of surface roughness radius of curvature on f when m is constant (Li and Guo, 2018). By studying the influence of different solid surfaces on ice heterogeneous nucleation, Eberle et al. (2014) found that the surface with air layer structure could delay ice freezing. Because of the micro-nano layered structure on the concave and convex solid surface, the size of r also has a great influence on f (Li and Guo, 2018).

As for the nucleation, it was first proposed more than 100 years ago by the American scientist Robert Gibbs. Through simple macroscopic energy analysis, he proposed that the formation of ice crystals must go through a stage of critical ice nucleus formation. If the critical ice nucleus did not form, this ice crystal could not be formed. "Classical nucleation theory" holds that phase transitions such as water freezing go through a nucleation process. That is, when supercooled water forms ice embryos, phase transformation will occur spontaneously only when the ice embryos formed reach the critical size, i.e. the critical ice nucleus. However, because the critical ice nuclei formation time is very short and the size of the critical ice nuclei is usually in the subnanometer scale, ordinary microscopes cannot observe (Luo et al., 2020). In recent decades, with the development of microscopic detection technology, many corollaries of classical nucleation theory have been confirmed. Whereas, some results beyond their expectations have also been found. In particular, the existence of the core concept of nucleation, critical nucleus, has not been provided with direct experimental evidence, thus hindering the further understanding of the important physical phenomenon of phase nucleation in nature. It even causes doubts about the practicality of the concept of critical nucleus at the micro level for macro-reasoning. To be specific, water freezing phase transition is attributed to the special complexity of water molecules and is closely related to our life. People have been looking forward to detecting critical ice nuclei for a long time. However, after many efforts, it has not been able to give clear results, which has become an outstanding basic problem in this field.

Wang et al. (Bai et al., 2019) creatively used GO nanoparticles with controllable size to detect the size matching signals of ice nucleation and nanoparticles, thereby detecting the presence and characteristics of microscopic transient critical nuclei. By studying the relationship between nanoparticle size and the ability of ice crystals to nucleate, the researchers found that ice nucleation was only promoted effectively when the nanoparticle size was larger than a certain critical value, whereas smaller nanoparticles hardly helped ice nucleation (Figure 5). Moreover, the size threshold phenomenon of nanoparticle size in promoting ice nucleation ability is common, which is inversely proportional to the supercooling temperature, and almost does not depend on the characteristics such as the structure type of nanoparticle. The experimental results are consistent with the prediction of the critical nucleus and free energy in the classical nucleation theory. The existence of the critical nucleus and the dependence of its size and supercooling temperature in the water freezing process have been experimentally confirmed for the first time. This study effectively clarified the widespread doubts in recent decades about the validity of "classical nucleation theory" in describing critical nuclear characteristics on the atomic scale and deepened the understanding of the microscopic mechanism of water freezing, as an important phase transition phenomenon. This work is of great significance to water freezing mechanism, phase transition phenomenon, and macroscopic and microscopic relations in statistical physics. At the same time, the strategy of detecting critical ice core can also be applied to the detection of critical nucleus in other phase nucleation processes, so as to improve the understanding of the whole phase nucleation field. In addition, the results show that the design of a patterned surface with the same size as the critical ice nucleus can effectively control the formation of ice crystals, which provides a new idea for the design of anti-icing coating.
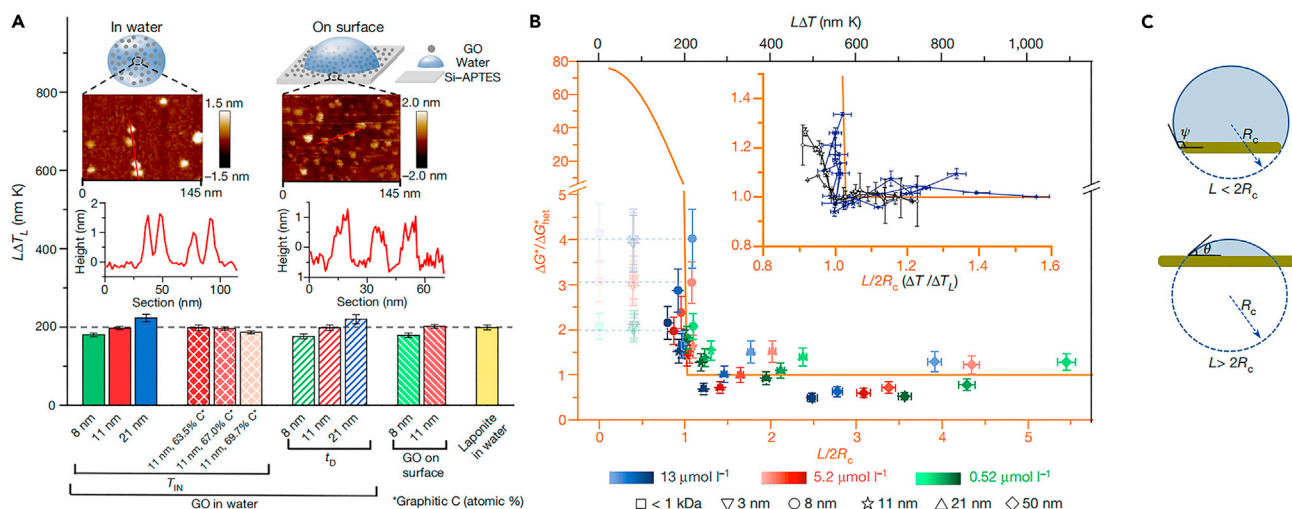
Figure 5. Transitions in nucleation activity of different nanosheet ice and mutations in free energy barrier of nucleation of GO nanosheet ice

(A) Schematic diagram of water droplets containing GO nanosheets or of water droplets deposited on substrates anchored with GO nanosheets, and the corresponding AFM image of GO.

(B) The functional diagram of $\frac{\Delta G^*}{\Delta G^*_{het}}$ and $\frac{L}{2R_c}$.

(C) Schematic diagram of the shape of the critical ice nucleus. Image reprinted with permission from (Bai et al., 2019).

SH ANTI-ICING MATERIAL

SH materials are regarded as one of the most promising materials for anti-icing applications because of their unique ability to repel or reduce contact with water droplets due to their micro-nano structure on the surface. By coating the surface with low surface energy materials to construct hydrophobic structures, or by chemical modification to hydrophobic structures, more materials can obtain superhydrophobicity (Dalawai et al., 2020; Qi et al., 2019; Wang et al., 2013). Based on many previous studies and reports, researches on the application of SH materials for anti-icing mainly focus on three aspects. The anti-freezing properties of SH materials are discussed in the following sections.

REMOVING SURFACE WATER DROPLETS BEFORE FREEZING

Since the discovery of the superhydrophobicity of lotus leaf (Jiang et al., 2004), rose petals (Bhushan and Her, 2010), and other petals, many researchers have imitated them to prepare SH materials with micro- and/or nano-scale textures on the surface. Quéré et al. proved for the first time that SHS has practical significance for anti-icing (Lv et al., 2014). It has a high WCA (>150°) and low CA hysteresis (CAH), and the microstructure of the surface texture contains concave angles (also known as protrusions or mushrooming structures). It is precisely because of this microstructure that air is trapped in the surface texture, resulting in negative Laplace differential pressure, which prevents the transition from the Cassie state to Wenzel state (Kreder et al., 2016) and causes the droplets on the surface to stay in the nonwetting Cassie-Baxter state (Cassie and Baxter, 1944; Shen et al., 2015b). When the impinging water drops fall on the SHS, the water droplets can contract on the SHS and bounce back to a certain height due to the extremely low CAH (Richard et al., 2002). Therefore, it is possible for droplets to be removed in a timely manner before/during the freezing on the SHS (Gauthier et al., 2015). In practice, water droplets hit the surface at various angles from different heights and with the corresponding kinetic energy. When such droplets hit the SHS, they immediately expand, then reach maximum deformation and contract, and finally bounce off the SHS. This process is shown in Figure 6.

Are SHSs ice resistant? First, its dynamic water repellency can be tested. Dynamic water repellency is considered as the first element for an anti-icing material because it reflects the ability to repel the incoming supercooled droplets. The dynamic water repellency performance was evaluated mainly by the contact time and contact process of the impacting droplet on the sample surface (Shen et al., 2019b). The contact time between the droplet and the surface determines the mass, momentum, and energy exchange between the solid and the liquid. Thus, reduced collision time can be beneficial in some applications, such
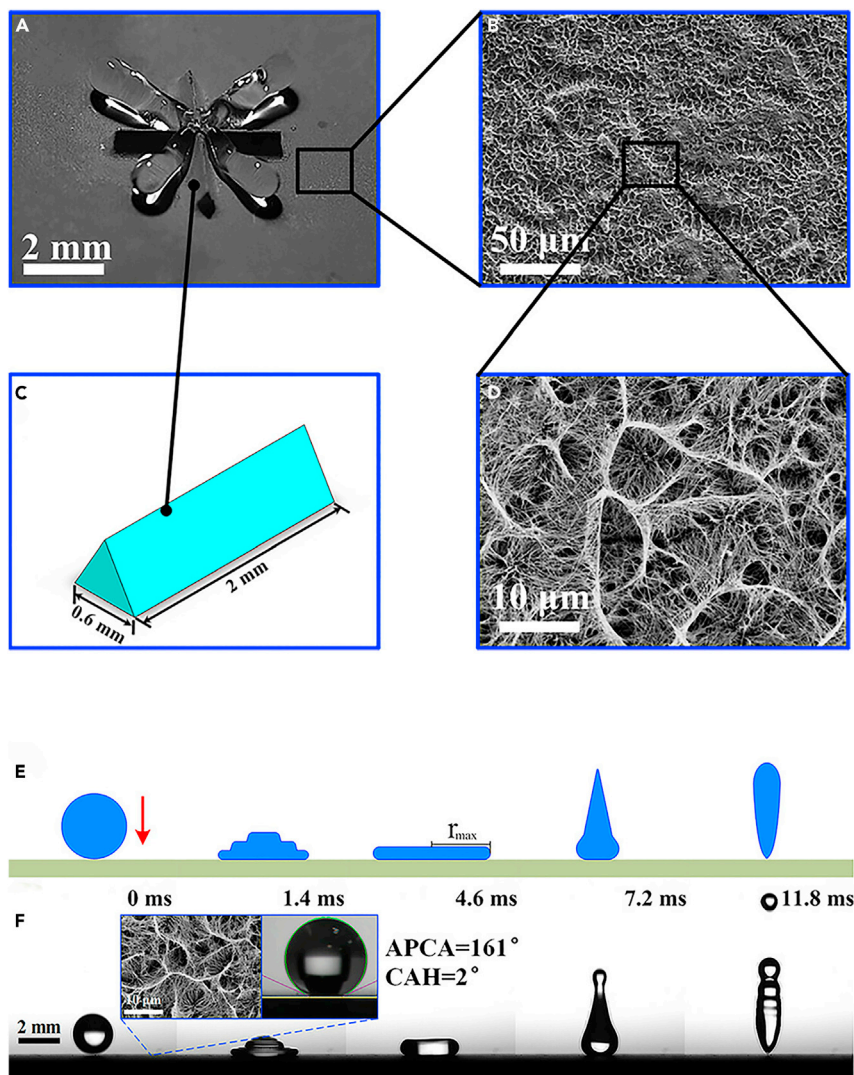
Figure 6. The primary ridge macrotextures and the Impact process of a water droplet on the sample surface

(A–D) The primary ridge macrotextures and morphologies on the sample surface.

(A) The impact water droplet on the SHS with the macrotexture.

(B) The field emission scanning electron microscopy (FE-SEM) image (×200) of the SHS.

(C) The schematic diagram of the equilateral triangle cylinder on the SHS.

(D) The FE-SEM image (×2000) of the SHS.

(E–F) Impact process of impinging water droplets on SHS.

(E) Schematic process of the movement process of the impacting water droplets on the SHS.

(F) Images recording the moving process captured via high-speed video; insets are the field emission scanning electron microscopy (FE-SEM) image of the SHS and the static image of a water droplet deposited on the surface. Image reprinted with permission from Shen et al. (2015b).

as anti-icing and anti-fogging. Droplet dynamics can be studied by using various dimensionless parameters (Yan et al., 2019b). For water droplets hitting the surface of lotus leaves, T. Schutzius et al. believe that the impact of water droplets can be characterized by the Weber number, which can be described by the following equation (Schutzius et al., 2015):

$$We = \frac{\rho_l U^2 D}{\gamma_{lv}}$$ (Equation 14)

where ρ_l is the density of the droplet, U is the velocity of impacting droplet, D is the diameter of the initial droplet, and γ_{lv} is the surface tension of the water-air interface.

Li et al. (2020) used laser expansion technology and chemical growth method to prepare ZnO nanorods micro/nano structure (Figure 7A), they observed the typical behavior of droplets striking the nanostructure/stratification (NS/HS) surfaces (such as NS-3 and HS-3 (Figure 7B) with different hydrophobic degrees at the different *We* values (Figures 7C and 7F). It is found that at the smaller *We*, the droplet underwent axisymmetric evolution, that is, diffusion, contraction, and oscillation after rebound, rather than adhesion to the droplet. In addition, they found that the rebounded droplets spread out a short distance in the radial direction before retracting inward, making the droplets stay in contact with the surface for a relatively long time. However, with the increase of the *We*, the rapid impact of the droplet causes its elongation stage to become unstable and oscillating, and its shape changes irregularly. The droplet deformation on the surface of NS-3 and HS-3 is similar. For a higher *We*, the deformation and oscillation of HS-3 is much calmer (Figures 7D and 7E). It is found that for the SHS with similar surface roughness, the work done by CAH is dominant. The smaller the CAH, the shorter the contact time. For NS surface, the CAH plays a leading role because the upward energy storage is not obvious. For HS surface, the interaction between the CAH and upward energy storage significantly shortened the contact time. Under different *We*, the variation of contact time is caused by the dynamic wetting state. The morphologic evolution of the elastic-droplet with *We* is dominated by the large vertical upward kinetic energy generated. It can be seen that the textured surface with low CAH and high energy storage is conducive to the rapid retreat of springback water droplets from the nonwet surface (Li et al., 2020).

Khanzadeh Borjak et al. (2020) used a high-speed camera to study the bouncing process of water droplets on a cylinder of SH glass (Figures 8A and 8B). In the experiment of SHS, it was found that by slowing down the lens when the Weber number varied between 27 and 161, the droplet with low Weber number would rebound when hitting the surface. During the bounce, the droplet spreads and contracts and falls off the surface. As the Weber number increases, the rebound regime becomes the splash-rebound regime. As can be seen from Figures 8C–8F, with the increase of Weber number, not only the number of secondary droplets but also the spreading diameter factor (the spreading diameter of the droplet in the azimuthal direction to the diameter of the primary droplet) of droplets on the surface of SH cylindrical glass increase significantly.

As for the asymmetric deformation of water droplets in the bouncing process, Tong et al. (2018) believed that it was caused by the interaction friction between the droplets and the surface, the gravity of the droplets, and other factors. In addition, he used the Ohnesorge number (Mundo et al., 1995) to explain the rebound dynamics of water droplets on the SHS. The formula is as follows:

$$Oh = \frac{\mu}{\sqrt{\rho \sigma D}} \qquad \text{(Equation 15)}$$

ρ, μ, σ, and D are the liquid density, viscosity, surface tension, and diameter of the impinging droplet, respectively. The rebound process needs to overcome the droplet's surface tension and self-weight. In the rebound process, ρ, μ, and σ are defined as fixed values due to the rebound dynamics between the SHS and the water drop interface. Therefore, the Ohnesorge number is mainly affected by the diameter of the impinged droplet. With the increase of the droplet size, the Ohnesorge number decreases. However, the small Ohnesorge number indicates that even at horizontal SHSs, the droplets rebound at lower heights (Tong et al., 2018).

Shen et al. (2019b) has prepared a high-performance SH fluorinated silica (F-SiO$_2$)@ polydimethylsiloxane (PDMS) coating by simple spraying process. The wettability of untreated (1) and treated (4) silica particles is shown in Figure 9A. When each is added separately to water, the treated silica particles are almost impossible to disperse into the water and instead float on the surface. As can be seen in Figures 9B and 9C, surfaces modified by silica become rough. This not only proves that they are hydrophobic but also demonstrates the successful modification of silica nanoparticles (Wu et al., 2018b). When an appropriate number of F-SiO$_2$ nanoparticles were added to the substrate of PDMS coating, the WCA on the coating was as high as 155.3°, and the CAH decreased to 2° as shown in Figure 9D (2). The resulting microstructure was almost able to well support the water droplets and make them have good water-resistance performance. This phenomenon can be explained by the Cassie-Baxter wetting model (Cassie and Baxter, 1944). In addition, Shen evaluates the dynamic water-repellency capacity of the SH coating by using two
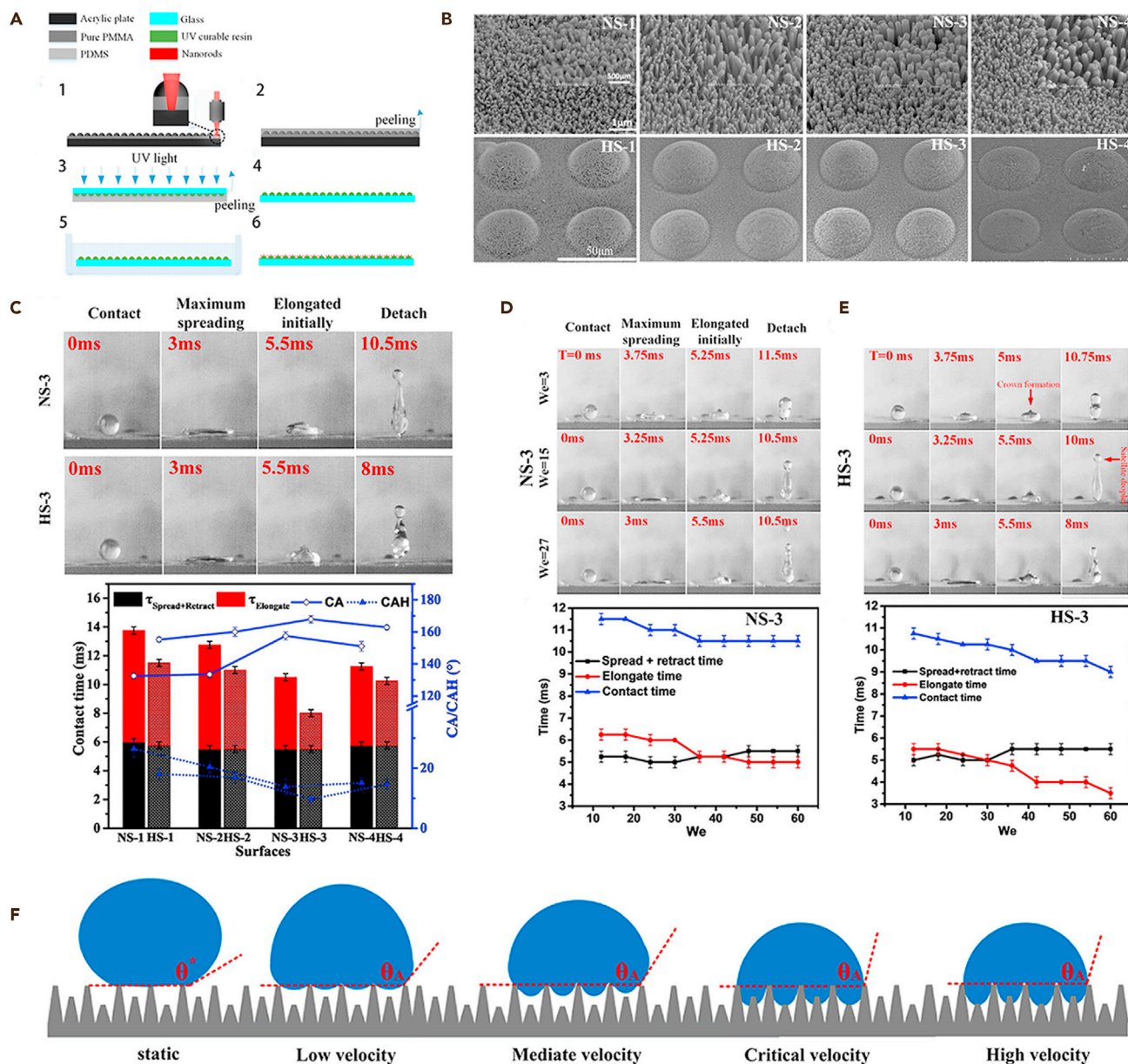
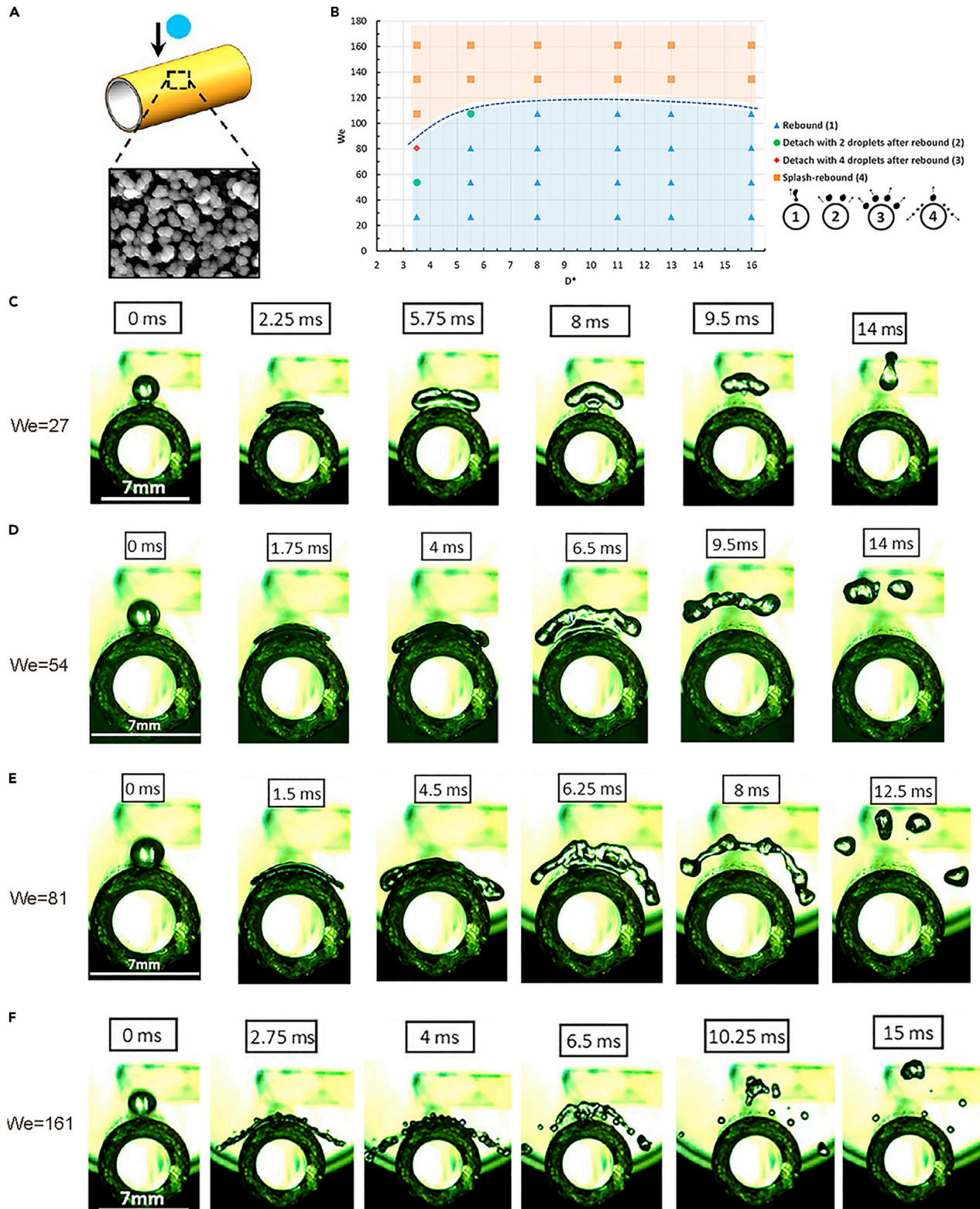**Figure 7. The impact dynamics of a droplet on two types of surfaces**

(A) Fabrication process of A micro-nanohierarchy: A micro-nanohierarchy was fabricated using the laser swelling technique and chemical growth of ZnO nanorods successively.

(B) Scanning electron microscopy (SEM) images of prepared surfaces: NS-1, NS-2, NS-3, and NS-4 are nanostructures fabricated by chemical growth, and HS-1, HS-2, HS-3, and HS-4 are micro-nanohierarchies built by a combination of laser swelling and chemical growth. The chemical growth times for both cases are 20, 30, 40, and 50 min, respectively. The insets show partial magnification. Image reprinted with permission from Li et al. (2019a).

(C) Selected moments for droplets impacting on NS-3 and HS-3. The moments include upon contact, maximum spreading, elongation initiation (starts from crown formation), and detach from the surface. In all cases, D_0 = 2.12 mm and We = 60.

(D and E) Time series of impacting droplets at different velocities. Selected moments for droplets impacting NS-3 and HS-3. Variations in contact time, spread, retract time, and elongate time with We for NS-3 and HS-3. For NS-3, a small steplike variation in the contact time appears at a We of 36. However, for HS-3, the contact time depends on the We; it decreases continuously and more remarkably with the We.

(F) Schematic of contact interfaces of impact droplets with different velocities on structured surfaces. Image reprinted with permission from Li et al. (2020).

A

B

- ▲ Rebound (1)
- ● Detach with 2 droplets after rebound (2)
- ◆ Detach with 4 droplets after rebound (3)
- ■ Splash-rebound (4)

C We=27

| 0 ms | 2.25 ms | 5.75 ms | 8 ms | 9.5 ms | 14 ms |

7mm

D We=54

| 0 ms | 1.75 ms | 4 ms | 6.5 ms | 9.5ms | 14 ms |

7mm

E We=81

| 0 ms | 1.5 ms | 4.5 ms | 6.25 ms | 8 ms | 12.5 ms |

7mm

F We=161

| 0 ms | 2.75 ms | 4 ms | 6.5 ms | 10.25 ms | 15 ms |

7mm

Figure 8. The impact process of water droplets on superhydrophobic cylindrical glasses

(A) Surface morphology of SH cylindrical glass. After heat treatment, nanoparticles of TiO_2 on the sample with SH feature after silanization.

(B) Diagram of the *We-D**, outcome regimes of the water droplet impact on SH cylindrical surfaces.

(C–F) Deformation of droplet rebound on an SH cylinder under different weber numbers. (C) *We* = 27, one secondary droplets after the rebound. (D) *We* = 54, two secondary droplets after the rebound. (E) *We* = 81, four secondary droplets after the rebound. (F) Splash-rebound: SH cylindrical sample, *We* = 161. Image reprinted with permission from Khanzadeh Borjak et al. (2020).

dimensionless parameters, Weber number and Reynolds number. The definition of Reynolds number is as follows:

$$Re = \frac{\rho_l D U}{\mu} \qquad \text{(Equation 16)}$$

In this formula, the parameters are consistent with the definition of the Weber number except that μ is the viscosity of the liquid. When the droplet with a radius of 1 mm hits the surface at a speed of 1 ms·s^{-1}, it can be calculated that *We* and *Re* are about 27.8 and 2,234.9, respectively. On the SH F-SiO$_2$@PDMS coating surface, the impingent droplets rapidly diffused (only 2.4 ms) and fully rebounded, with a retracting time of 7.8 ms. Therefore, the total contact time from contact to disengagement of the impinged droplets is 10.2 ms (Figure 9E). The impacting droplets can bounce off the SH F-SiO$_2$@PDMS coating surface even at the lower temperatures of −5°C and −10°C, powerfully demonstrating excellent dynamic water repellency at low temperatures (Figures 9F and 9G) (Shen et al., 2019b).

Wang et al. (2019a) found that when a droplet hit an SHS, the kinetic energy of the droplet's impact was transferred to the surface energy, enabling the droplet to completely rebound from the surface. The droplet remains spherical after the first impact, then bounces back and forth in free fall before sliding off the surface or remaining spherical. Wang used the same SHS to squeeze the water droplets on the surface. The droplets on the SHS only changed from spherical to ellipsoid without wetting the surface. When the SHS was removed, the water droplets returned to spherical again. It can be seen that the droplet presents Cassie state (Cassie and Baxter, 1944) on the SH solid surface, rather than Wenzel state in wet contact model (Wang et al., 2019a).

So far, research on SHS has found that there have been a lot of SHS s with different materials. However, can the same situation be found on the surface of SH materials with different structures?

Chu et al. (2020) took advantage of graphene-based micro-nano fractional structural membranes modified by FDTS (1H, 1H, 2H, 2H-perfluorodecyl trichlorosilane) to study the bounce of droplets on the surface. Compared with the four films (Figure 10A) with different structures (Figure 10B), which are FDTS-modified rGO smooth film (S-FGF), FDTS-modified rGO film with nano-SiO$_2$ particles decoration (N-FSGF), FDTS-modified microstructured rGO wrinkled film (M-FGF), and micro-nano hierarchical structure SiO$_2$/rGO film (MN-FSGF), the WCA of MN-FSG is 152.1°, and the SA of MN-FSG is 2.3° (Figures 10D and 10F). The surface shows good SH properties, which conforms to the Cassie-Baxter equation (Cassie and Baxter, 1944).

Moreover, it is found that under the conditions of low Weber number (*We* = 27.4) (Lagubeau et al., 2012), ambient temperature −10°C, and 50 ± 5% relative humidity, 4.2 μL water droplets fall in free from a height of 50 mm above the surface. The water drop hits the surface, spreads to the maximum, and experiences repulsion and rebound (Figure 10C). Compared with the films with four different structures, the maximum rebound height of water droplets on the surface of MN-FSGF film can reach 6.6 mm, which has excellent waterproof performance. This is due to the work done by the adhesive force between the solid surface and the liquid. In addition, by exploring the influence of different heights on MN-FSGF in the dynamic process of droplets (Figure 10E), it is found that droplets of different heights can rebound on the surface, and the kinetic energy of droplets increases with the increase of the initial height of droplets. Therefore, the maximum spreading diameter of droplets also increases. In addition, by analyzing the freezing process of liquid droplets of the same volume on four different film surfaces in Figure 10G and the histogram of freezing delay time in Figure 10H, it can be found that MN-FSGF has better anti-icing performance. In addition, the temperature-sensitive resistance of the micro-nano graded structure membrane enables it to have low-temperature, self-sensing ability, which can sense the influence of water drops (5°C) and detect water drops of different height and size at −10°C. This is of great significance in the field of ice monitoring and real-time de-icing (Chu et al., 2020).
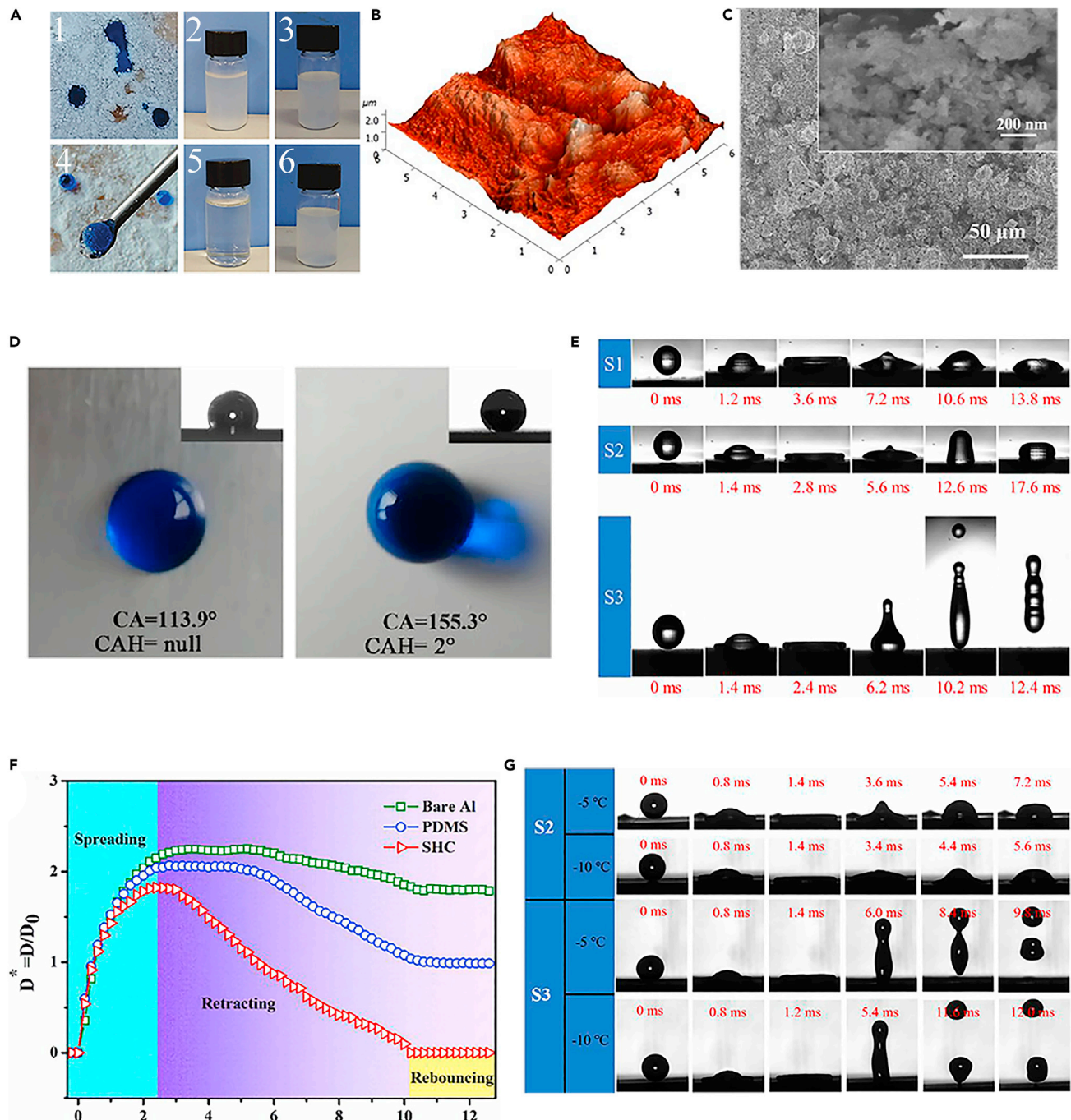
Figure 9. The impact process of water droplets on a kind of high-performance SH F-SiO$_2$@PDMS coatings

(A) Photographs of water droplets on (1) raw SiO$_2$ and raw SiO$_2$ dispersed in water (2) and ethanol (3). Photographs of water droplets on (4) F-SiO$_2$ and F-SiO$_2$ nanoparticles dispersed in water (5) and ethanol (6). Image reprinted with permission from Wu et al. (2018b).

(B) AFM 3D surface topography of the SH F-SiO$_2$@PDMS coatings.

(C) SEM images of SH F-SiO$_2$@PDMS coatings, and inset is the high-resolution image.

(D) The photographs of 8 μL water droplets on (1) PDMS coatings and (2) SH F-SiO$_2$@PDMS coatings. Insets are 4 μL droplets for measuring CA and CAH.

(E) Time-lapse photographs of 4 μL water droplets impacting on bare aluminum (S1), PDMS coatings (S2), and SH F-SiO$_2$@PDMS coatings (S3) at room temperature.

Figure 9. Continued

(F) The dimensionless parameter of spreading factor ($D^* = D/D_0$, where D_0 is the original diameter of droplet, and D is the diameter of droplet in contact area with the surface) versus time after the droplet touched the surface.

(G) Time-lapse photographs of 4 μL water droplets impacting on (S2) PDMS coatings and (S3) SH F-SiO$_2$@PDMS coatings at −5°C and −10°C. Image reprinted with permission from Shen et al. (2019b).

Wang et al. (2021a) prepared the SHS of silicone rubber by means of a simple direct replication and compression molding process (Figures 11A). The surface has holes of varying sizes (as show in Figures 11B and 11C). The WCA was 158.5 ± 0.5° and the rolling angle was 8.9 ± 0.1°. As can be seen from Figures 11D and 11E, the water droplets on the surface of silicone rubber are spherical, and the water droplets can be moved easily. A high-speed camera showed that water would bounce off the SHS of the silicone rubber (Figures 11F). When the droplet falls perpendicular to the surface, there is no negative correlation between the droplet contact time on the surface and the droplet falling height. However, when the droplet falls into the SHS at an angle of 30° in the horizontal plane, the bouncing times and rolling time are negatively correlated with the falling height (as show in Figures 11G and 11H) (Wang et al., 2021a). This is beneficial to the preparation of self-cleaning SH-moulded silicone rubber products.

Khadak et al. (2020) combined a polymer-based coating with a silica topcoat with the prepared carbon-fiber-reinforced composite to obtain a layered SH-coated carbon-fiber-reinforced material. In coating tests, its WCA was stable and durable. The maximum WCA of the material was 163°, showing strong static non-wettability and excellent dynamic water repellent, forcing water droplets to bounce off the surface in less than a second. It can roll water droplets on the surface by tilting, blowing, or mechanical vibration and can even easily remove ice that forms on the surface (Subeshan et al., 2020).

According to the above examples and analysis, because of low liquid-solid adhesion, the droplet can completely rebound when hitting the SHS. Therefore, the SHS has a certain ability to prevent the impinging water droplets from freezing on the surface. The rebound behavior of the droplet on the SHS is directly related to the ice resistance, because it determines the contact time and contact area of the liquid-solid interface. However, with the exception of water droplets struck by a surface, water vapor condenses rapidly in wetter environments by contacting with a cooler solid surface and condenses into water droplets. For this type of water droplets, what is the self-cleaning ability of the SHS?

Although the water droplets condensed on the surface do not have the same initial kinetic energy as the water droplets impinged on it, as an SHS, there is a large amount of air trapped between the micro and nano surface structures. When the condensate is formed on the SHS, the small radius of the synaptic tip makes the droplet have a larger CA with the surface and a smaller CAH, so that the contact area between the droplet and the surface is minimized (Ensikat et al., 2011; Qi et al., 2020b). The interaction between water droplets and the surface is weak, and the water droplets remain spherical (Vandadi et al., 2019). Moreover, air can effectively act as a thermal barrier between the SHS and the water droplets, so that the water droplets on the SHS remain in the Cassie-Baxter state (Barthwal and Lim, 2019; Cassie and Baxter, 1944). In this way, the water droplets are easily pushed off the surface by external forces, thus preventing them from freezing. Back in 2013, Boreyko discovered that droplets of agglutinate jump on their own on SHS (Boreyko and Collier, 2013). Barthwal (Barthwal and Lim, 2019) found that this jumping motion is caused by two or more droplets coming together in contact and then jumping off the SHS as the droplets release excess surface energy on the low-adhesion SHS (Figure 12). Barthwal compared the SH dual-shape micro-/nanostructured (MN-) Al surface, bare Al surface, and silicone oil-infused PDMS coating (SLIPS) on the MN-structured Al substrate and observed the vapor condensation processes on the three surfaces under the same conditions (0°C). It is found that the size and coverage of water droplets on the SHS are much smaller than those on other surfaces, and the droplets still remain spherical. This is due to the SHS of this micro/nano dual structure, which generates a large amount of air between the micron and nano structures. This greatly increases the gas-liquid interface, prevents condensed water droplets from penetrating into the cavity, and maintains the Cassie state (Cassie and Baxter, 1944). In addition, when the ambient temperature is −5°C, with the passage of time, in the central region area of the SHS, tiny droplets gather to form microdroplets, which almost remain in the liquid state. The droplet's automatic migration reduces the size and surface coverage of the condensation droplets, thus delaying the time of surface freezing or frosting. However, when the ambient humidity increases or the substrate surface temperature decreases, not all the droplets condensed on the SHS s will migrate or even jump, and the water droplets on the surface will be in the Wenzel state of high adhesion (Miljkovic et al., 2013).
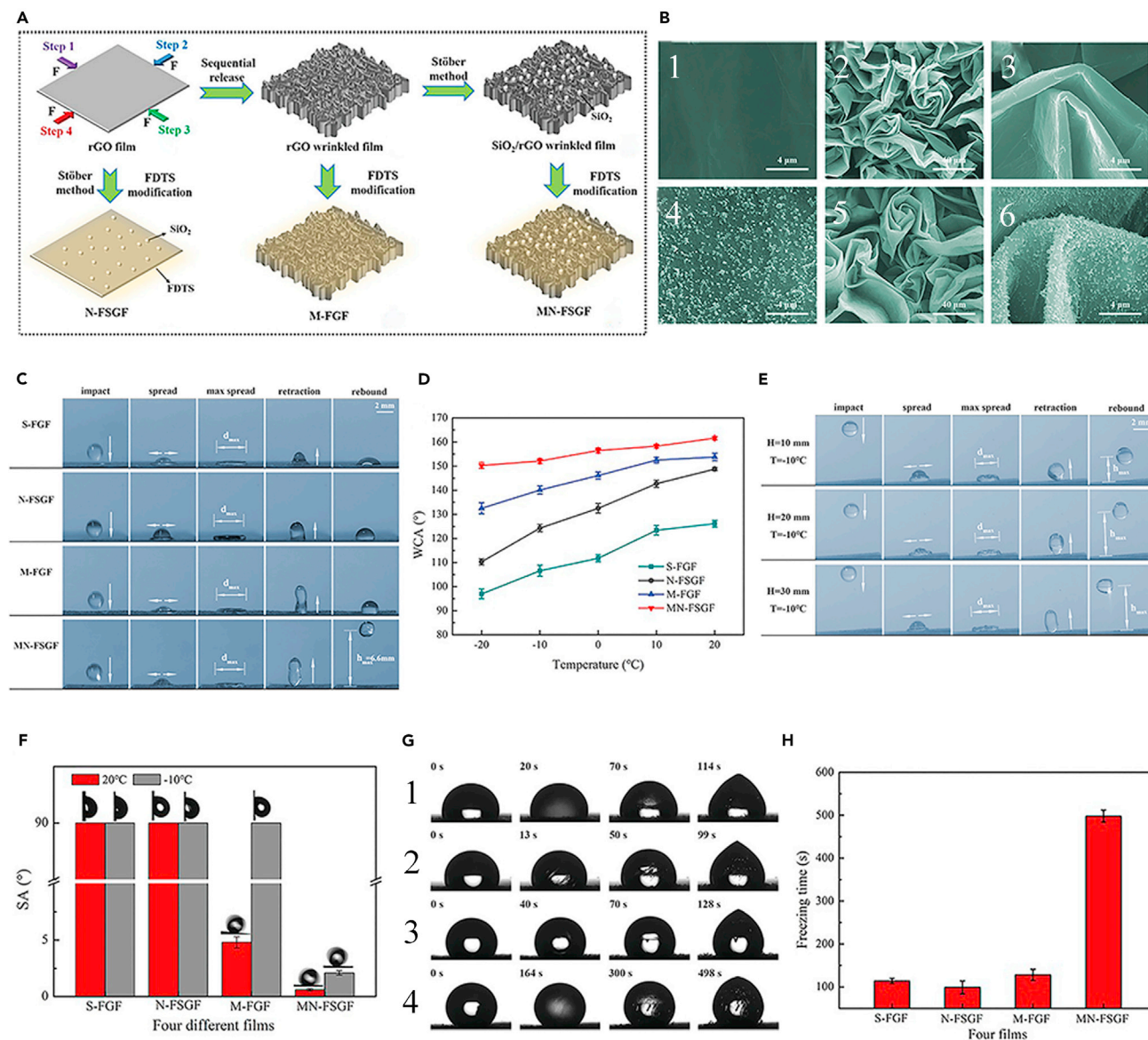
Figure 10. The wettability of four different structures and the dynamic impact process of droplets

(A) Schematic illustrations of preparing four films with different structures. The first is rGO synovium S-FGF; the second method is to use FDTS to modify the rGO film to get M-FGF; the third method is to use FDTS to modify SiO_2/rGO films to obtain N-FGF; the fourth is to use FDTS to modify SiO_2/rGO wrinkled film to obtain MN-FGF.

(B) SEM images of four different structures. (1–2): the detailed morphology of S-FGF and M-FGF, respectively. (3): highly magnified SEM images of 2. (4–5): the detailed morphology of N-FSGF and MN-FSGF, respectively. (6): highly magnified images of 5.

(C) The dynamic impact process of water droplets on the four films at temperatures of −10°C and RH of 50 ± 5%.

(D) The WCA of the four films at different temperatures from +20 to −20°C.

(E) Dynamic process of water droplets impact on the MN-FSGF from different heights at temperature of −10°C and RH of 50 ± 5%.

(F) The SA of the four films at 20°C and −20°C.

(G) The freezing process of 7 μL water droplets on four surfaces and the delay of freezing at −10°C.

(H) The column diagram of delayed icing time after multiple icing experiments on four surfaces. Image reprinted with permission from Chu et al. (2020).

In order to realize the self-hopping phenomenon of small-scale condensed droplets, the SHS structure must meet three criteria (Gong et al., 2017). First, the spacing between the convex pillars on the surface should be as small as possible, such as micro-nano scale, to avoid water penetration (Mouterde et al., 2017). Second, the tip size should be as small as possible to minimize interface adhesion. Third, the convex

Figure 11. The impact process of water droplets on the SHS of silicone rubber

(A) Flow chart of preparation of SHS.

(B) SEM image of silicon rubber surface.

(C) 3D morphology of silicone rubber surface.

Figure 11. *Continued*

(D) Different volume of water droplets in contact with the surface of sample A (the silicon rubber with special surface structure prepared by the direct copy method) of the picture.

(E) The whole process of contact, deformation, and departure of the droplet from the surface of sample A.

(F) 1, 2, and 3 are the movement process of droplets falling to the surface of sample A from the height of 5 mm, 5.5 mm, and 8 mm, respectively.

(G) Bar chart of falling height, maximum spreading diameter, contact time, and maximum bouncing height of sample A.

(H) I, II, and III represent the drop height 7, 5, and 3 mm, respectively, the movement of the droplet from contact with the sample A to leave; IV,V and VI represent the drop height 7, 5, and 3 mm respectively, the movement of the droplet from contact with the sample B (the original silicon rubber) to leave. Image reprinted with permission from Wang et al. (2021a).

pillar on the surface has a certain height or depth to prevent the droplet bridging fracture (Xing et al., 2020). In addition, droplet jumping behavior depends on multiple droplet merging, so at least one adjacent droplet must be present (Yan et al., 2019a). Yan et al. (2020) found that the Laplacian pressure difference caused by the SHS structure was a potential driving force for droplet jumping. Although the self-removal of condensed droplets on SHS is energy saving, its efficiency depends on the growth rate and coalescence frequency of condensed droplets. Generally speaking, the faster the growth rate and the more frequent the aggregation, the higher the self-removal efficiency of the condensed droplets. Inspired by the special hydrophilic/hydrophobic structure on a beetle's elytra, He et al. (2013) prepared a layered micro/nano-pore structure on the surface of aluminum by the method of micro-contact printing and chemical bath deposition and modified the surface with polyvinyl alcohol (PVA). Water vapor condenses into droplets mainly in micropores arranged in a hydrophilic polymer modification. Because of the layered surface nanopores, the aggregated droplets on the surface are in a stable Cassie state (Cassie and Baxter, 1944; Lafuma and Quere, 2003). When the PVA is adsorbed in the micropores, the condensed droplets can easily rise to the top of the micropores, and the SHS of the pores can also achieve controlled and rapid self-removal. The synergistic effect between the SH layered porous surface and the PVA adsorbed in the micropores directly promoted the rapid nucleation, controlled coalescence, and efficient self-removal of water.

Zhang et al. believes that nanostructures with lower surface energy, sufficiently narrow surface spacing, and longer verticality can improve the mobility of the surface droplets because there is less pinning of condensation droplets on such surfaces (Zhang et al., 2017). Wen et al. reported a novel layered SHS with micro-patterned nanowire arrays that can spatially control the initial nucleation of moving droplets through tightly spaced nanowires. The use of micro-patterned nanowire arrays facilitates the spontaneous outward movement of droplets for rapid droplet removal (Wen et al., 2017). In addition, Lee et al. (2018a) proposed an SH material based on the magnetic response type layered hair array, which was capable of adjusting the bending state of the hair array structure through the external magnetic field to induce various droplet bouncing behaviors in different modes, which was able to effectively remove water droplets on the surface and effectively prevent surface icing behavior (Lee et al., 2018a). In addition, Shen et al. (2018) found two kinds of SHSs, which were layered nanoporous structures and open nanocone structures. They make the condensed droplets have high dynamic self-propelling ability (Yan et al., 2019a). It has been reported that the self-migration of condensed droplets on SHSs will be weakened by droplet microscopic pinning effect (Smith et al., 2018). As we all know, when the ambient temperature drops to 0°C, it is inevitable that water freezes into ice. SHS can remove water droplets before the surface water droplets are still frozen. If the freezing rate is greater than the surface water droplets removal rate, the water droplets will freeze on the surface. During the development of SH materials, many studies have reported that SHSs can prevent freezing by delaying the freezing time, which will be analyzed in the next section.

CONTROLLING ICE CORE FORMATION

Generally, when the temperature is below 0°C, the water droplets stay on the surface long enough that they usually nucleate and freeze (Jin et al., 2018). It can be seen from the previous section that the SHS has a strong water-repellency performance, and the water droplets can be removed from the surface in time before the water droplets freeze. Then, if in the case of abrupt temperature decrease, water droplets have not been removed in time, or heterogeneous nucleation occurs on the surface under the influence of dust and other impurities, can the SHS have good de-icing performance? According to Equation 12, it is found that $f(\theta)$ increases with the increase of θ. Therefore, when θ increases, the nucleation free energy barrier is bound to increase, delaying the formation of ice nuclei in water droplets (Zhan et al., 2014). Now the question arises: where is the ice nucleation in the droplet? To solve this problem, Liu et al. (2020a) used a three-dimensional computational fluid dynamics (CFD) model to study the morphological changes of the droplets and simulate the phase transition of the droplets on the SHS (Figure 13). The freezing process of a
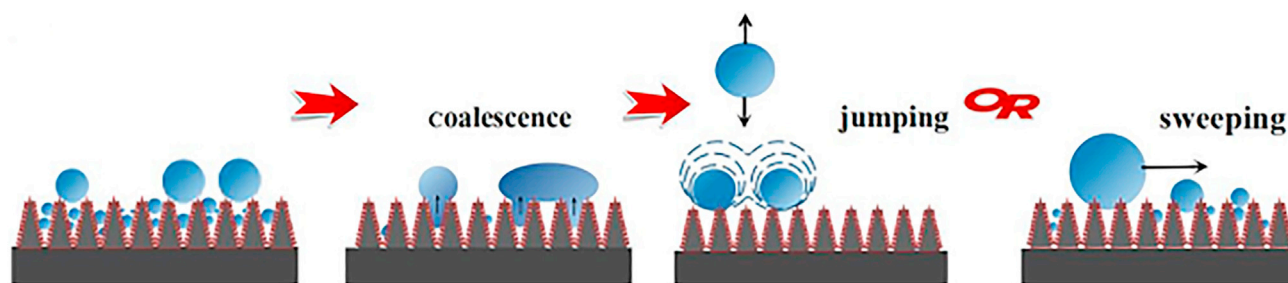
Figure 12. Schematic diagram of droplet self-propulsion induced by coalescence on SHS
Schematic illustrations of coalescence-induced self-propelling including bouncing and sweeping on the SH open nanocone structure surface. Image reprinted with permission from Shen et al. (2018).

single droplet on different wetting surfaces was simulated and compared. The SHS has higher surface roughness and lower surface free energy. The higher surface roughness leads to a larger static CA (>150°), whereas the lower surface free energy leads to a lower ice adhesion force (Wu et al., 2018a) and a lower freezing probability (Wu and Chen, 2018; Wu et al., 2019b), which can theoretically delay surface freezing.

From the thermodynamic point of view, the freezing process on the SHS is mainly due to the rapid heat exchange at the solid-liquid interface after the supercooled droplets contact with the solid surface. Is it possible to delay the freezing behavior of droplets on the surface by influencing the heat transfer process? The answer is yes. According to Fourier 's law, the heat transfer (Q) between a supercooled water drop and a surface can be written as:

$$Q = \int_{T_1}^{T_2} KSdT$$

(Equation 17)

In this formula, T_1 and T_2 are the supercooled water droplets and surface temperature, K is the heat transfer coefficient, and S is the solid-liquid contact area (He et al., 2011). Moreover, the freezing rate of the droplets in contact with the surface is strongly related to the heat transfer rate of love between the supercooled droplets and the substrate. The heat transfer rate of the two surfaces can be described by the following equation:

$$\frac{dQ}{dt} = -KS\left(\frac{dT}{dx}\right)$$

(Equation 18)

where dQ/dt is the heat transfer rate (J/s) and dT/dx is the temperature gradient. In order to reduce the heat transfer efficiency, it is necessary to reduce the heat transfer of the actual supercooled droplets after contacting with the surface. According to the formula, materials with low heat transfer coefficient can be selected to delay the formation of ice on the surface. For example, paraffin wax with very low thermal conductivity can be used as a heat insulating material to delay heat diffusion. Duc and Binh (2020) chose paraffin as the raw material of the coating due to low thermal conductivity and easy coating. The moth eye structure was first fabricated on the quartz substrate and then covered with paraffin to prepare an SH nanostructure-coated paraffin (NSP) surface. The paraffin layer sits only at the top of the nanostructure, separating it from the outside environment and effectively preventing the droplets from transferring heat to the cold substrate. Experiments showed that the NSP surface had a longer freezing time than the exposed coating, about 300 s. This is due to the combination of an air trap and a paraffin layer on the NSP surface, which minimizes heat transfer per unit time and thus extends the freezing time (Duc and Binh, 2020).

By inquiring the thermal conductivity table, it was found that thermal conductivity: metal > oxide. In addition, the air has a lower thermal conductivity (Fan et al., 2019). Based on the composite structure of taro leaf, Liu et al. (2020b) fabricated the micro-pillar array structure (MPA) on Ti_6Al_4V substrate by direct laser interference lithography (DLIL) and grew a layer of nano-grass structure (NG) on it by hydrothermal treatment. Experiments show that the layered composite structure not only has good SH properties, but also has an apparent CA of 172° and the SA of 4°. At −10°C, the delay time of water droplets freezing on the surface is 3,732 s. This is due to its high CA and small contact area at low temperature, and its surface layer is a TiO_2
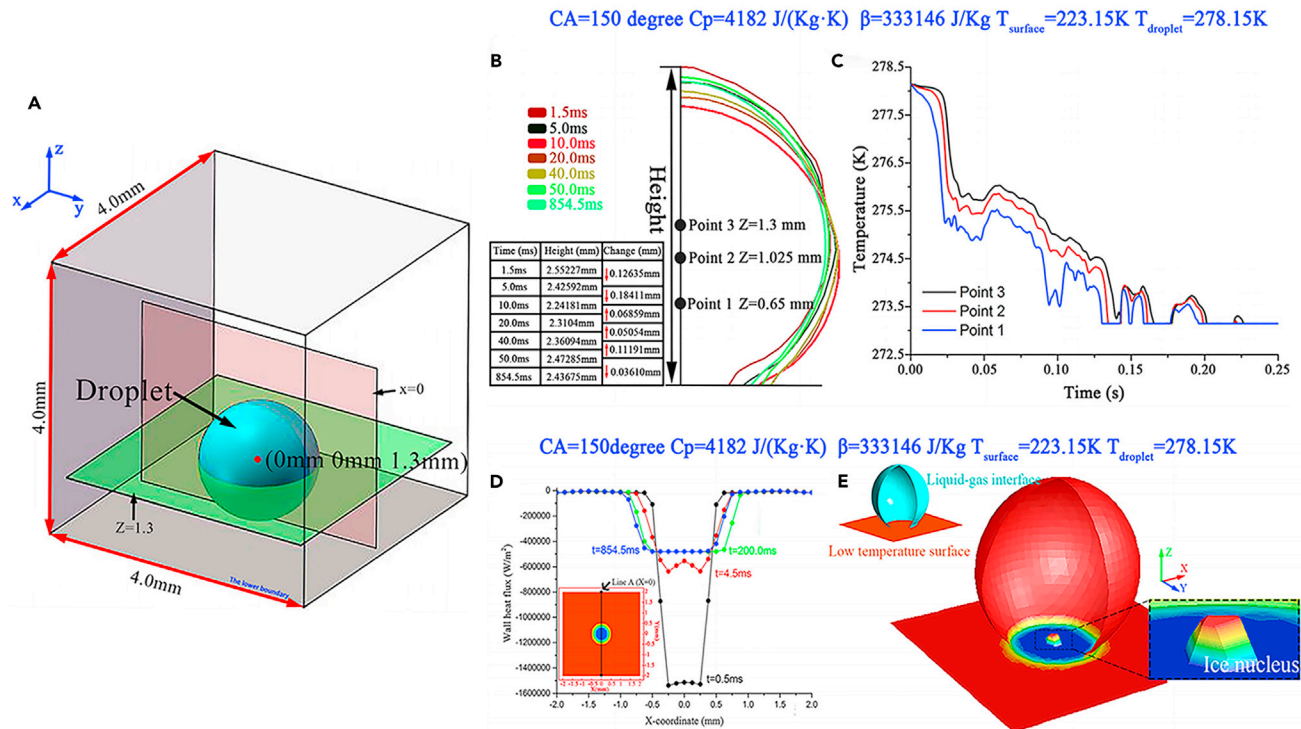
Figure 13. Schematic diagram of theoretical model of droplet morphology change
(A) The mathematical model of computational domain.
(B and C) The morphology change of droplet (B) and the temperature variation inside the droplet before freezing (C). The formation of ice nucleation.
(D and E) Wall heat flux change curves at different moments. (E) The position of ice nucleation at 854.5 ms. Image reprinted with permission from Liu et al. (2020a).

nanostructure with low thermal conductivity. Moreover, the layered structure of the surface provides balloon formation and reduces the CAH. Therefore, the SH structure can be used for anti-icing, anti-frosting, or anti-fogging on the surface of titanium alloy (Liu et al., 2020b).

Some researchers have found that due to the special structure of the SH material on the surface, when the droplet stays on the surface of the SH material, the solid-liquid-gas coexistence interface will be formed between the SHS and the droplet (Yin et al., 2020). Due to the low heat transfer efficiency of air, the water droplets trap the air below to form an air cushion, which becomes an effective barrier, greatly reducing the contact area with the water droplets and preventing heat transfer from the droplets to the matrix, further extending the freezing time and improving the anti-icing performance (Jiang et al., 2018). It is found that the microstructure of SHS is an important factor affecting its anti-icing. In addition, the thermal barrier formed by the air cushion (air pockets) between the SHS and the supercooled water droplets can reduce the degree of supercooling of the droplets, resulting in a lower freezing temperature of the droplets (Liu et al., 2019c). In addition, the contact area between the droplet and the solid surface is sorted as Smooth > Micro > Nano > Hierarchical (corresponding to the WCA $0° < 150.3° < 156.4° < 163.4°$). Therefore, the degree of heat transfer is suppressed to Smooth < Micro < Nano < Hierarchical (He et al., 2020). It can be seen that the SHS with nanostructure or hierarchical structure has significant anti-icing ability. Sarshar et al. also demonstrated that smaller nanostructures can enhance the anti-icing effect of layered SHSs (Sarshar et al., 2018).

Xiang et al. (2020) found that TiO_2 pinecone-like microstructures/nanostructures prepared by stearic acid modification on Ti substrates have certain SH properties. An air layer is formed between the water drop and SHS, which can effectively hinder heat transfer. Moreover, the contact area between the SHS and the water drop is smaller than that of the superhydrophilic surface, which reduces the freezing rate of the water drop on the surface and makes it difficult for the droplets to freeze on the surface (Li et al., 2018). This indicates that the slow freezing time and the low interaction force between the ice particles and the sample surface
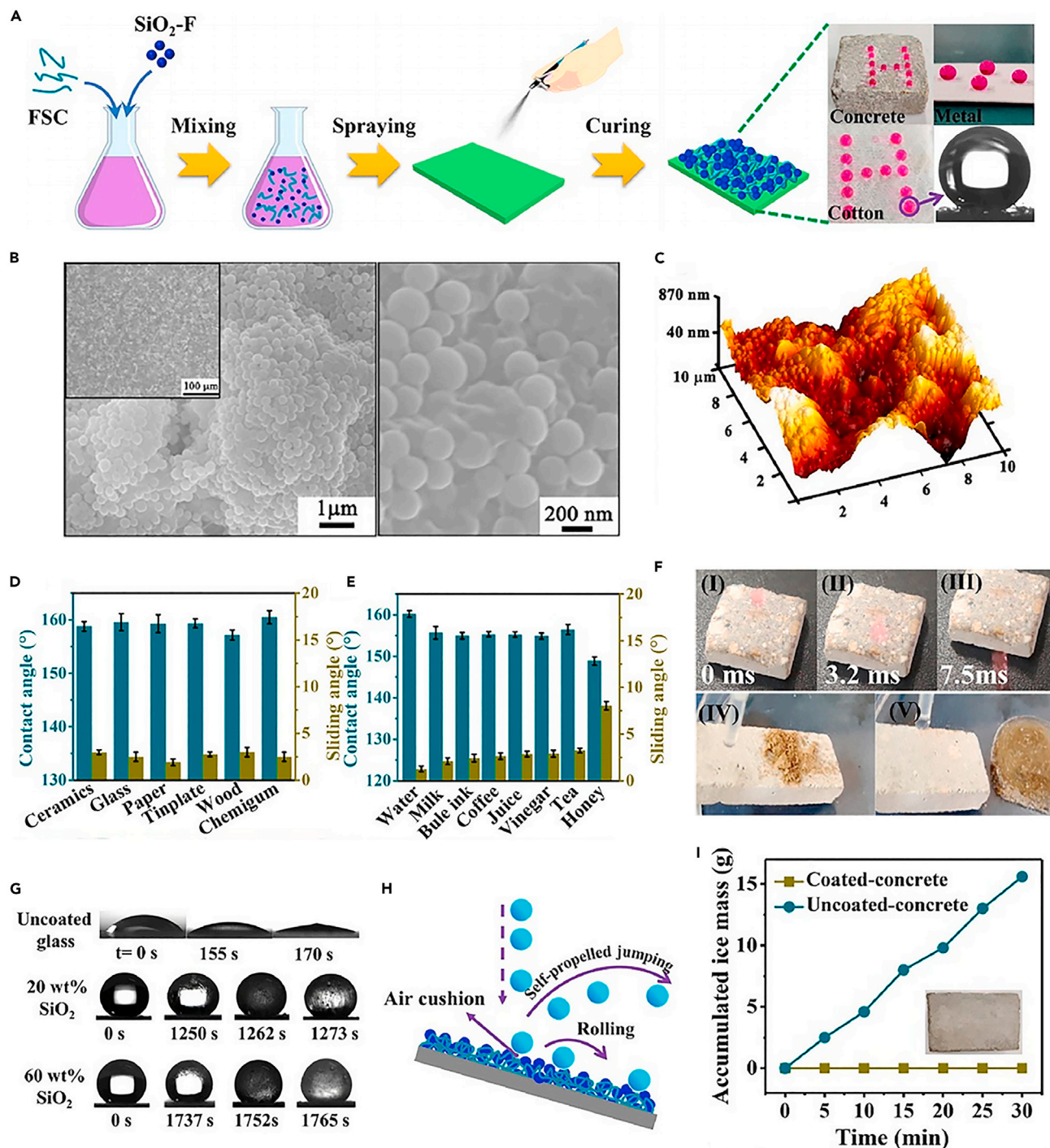
Figure 14. Study on SH and anti-icing properties of FSC/SiO$_2$ coatings
(A)Spraying process of FSC/SiO$_2$ SH coating and superhydrophobicity shown on concrete, metal, and cotton.
(B) SEM images of FSC/SiO$_2$ composite coating with 60 wt% SiO$_2$–F.
(C) AFM phase diagram of SH composite coating.
(D) WCA and SA of different coated substrates.
(E) WCA and SA of different water droplets on the coating surface.

Figure 14. *Continued*
(F) Water repellence and self-cleaning performance of the coated concrete: (I ∼ III) Sequential images of the dynamic behaviors of 7.25 μL water droplet impacting on the anti-icing surface from a height of 10 cm.
(G) Photographs showed dynamic icing process of 2 μL water droplets on the untreated and FSC/SiO_2–F coated surface at −20°C.
(H) Schematic illustration of the cold-rain simulated experiments.
(I) A function of the amount of ice accumulated on the surface and the treatment time. Image reprinted with permission from Wu et al. (2020).

can determine the anti-icing performance (Li and Guo, 2018). It also indicates that the TiO_2 SHS can delay the freezing time and exhibit good anti-icing performance.

In the study of SH Ni-Cu-P coating, Wang et al. (2019b) also found with environmental scanning electron microscopy (ESEM) that there were air pockets on the surface of the coating, which helped to form a solid-liquid interface with a smaller contact area, reducing heat exchange (Bhushan and Chae Jung, 2007). When water droplets freeze on the surface, the smaller the water-solid contact area, the lower the liquid-solid nucleation rate. XPS analysis shows that the hydrocarbon groups adsorbed by Ni-Cu-P coating may also form a thin low surface energy layer at the interface, which provides an additional barrier for water droplets and effectively reduces the interface contact between water droplets and the coating, preventing the formation of interlocking ice. Through the droplet icing test, the freezing time of water droplets on the surface of Ni-Cu-P coating is prolonged significantly, and the freezing intensity decreases sharply. It can be seen that the SHS also has good anti-icing performance.

Wu et al. (2020) deposited hydrophobic silicon fluoride particles and fluorinated-silicon-based copolymer (FSC) uniformly on the substrate surface through spray curing, forming a nanoscale layered structure that mimics the structure of lotus leaves (Figure 14A). According to SEM and AFM analysis, the phase separation of the multifunctional copolymer containing siloxane units forms micro-bulges on the surface, which not only increases the surface roughness but also the graded micro-nano structure allows more air to be trapped between the liquid/solid interface, forming an air capsule. Reduces the surface energy of the coating (Figures 14B and 14C) (Liu et al., 2019d). In addition, the FSC/SiO_2-F composite coating can be applied to a variety of surfaces. With the exception of honey droplets, the droplets commonly used in everyday life show high CA of more than 150° and low SA of less than 5° on the coating surface (Figures 14D and 14E). As shown in Figure 14F, the coating exhibits excellent water repellency. Combined with the cold rain impact surface test in Figure 14H, water droplets hit the surface of the coating, and it is easy to rebound or roll off. This helps keeping the surface from freezing. Figure 14G shows the dynamic freezing process of 2 μL water droplets on the coating surface at −20°C. It can be seen that FSC/SiO_2-F composite coating can delay the freezing time of water droplets. The freezing time of especially high SiO_2-F content (60 wt%) is almost 10 times that of the uncoated coating. By contrast, the ice accumulation on the surface of FSC/SiO_2-F composite coating is much less than that on the uncoated surface in the same time (Figure 14I). The main reason is not only the increase of the free energy barrier of nonuniform nucleation on the surface of the SH coating but also the decrease of the contact area of the surface due to the hierarchical micro-nano structure, which leads to the decrease of the heat transfer rate. Moreover, the siloxane group in the copolymer has high structural stability under harsh environment, which improves not only the adhesion between particles and substrate but also the chemical/mechanical stability of the SH coating (Liu et al., 2019e; Shen et al., 2019b; Zhang et al., 2019b). It can be seen that the SH coating not only has good water repellency but also has a certain anti-icing performance.

Sun et al. (2020a) prepared SH aluminum alloy samples by combining high-speed wire discharge machining and short-time chemical etching method with modification treatment. The preparation time was shortened from 20 h to 8 h by the introduction of chemical etching. It can be seen from Figures 15C and 15D, the CA of the SH aluminum alloy sample prepared was 158.6 ± 1.3°, and the SA was less than 1°. In combination with Figures 15A and 15B, it can be found that the surface of the SH aluminum alloy has micro-nano-sized holes and depressions. In addition, the chemical composition of 2m-8h Al alloy samples was analyzed by XPS (as shown in Figure 15E). The presence of fluorine indicated that PFOA was successfully grafted onto 2m-8h Al alloy samples. Low surface energy micro/nano structures can produce ideal SH properties. Therefore, 2m-8h Al alloy sample has the best superhydrophobicity. It has been reported that the freezing time delay test can well explain one of the important methods of ice resistance under the condition of supercooling (Lei et al., 2019). In the temperature range of −12 to 24°C, the freezing delay time of smooth aluminum alloy and SH aluminum alloy was tested, and it was found that the time of water drop on the average frozen smooth aluminum alloy sample decreased
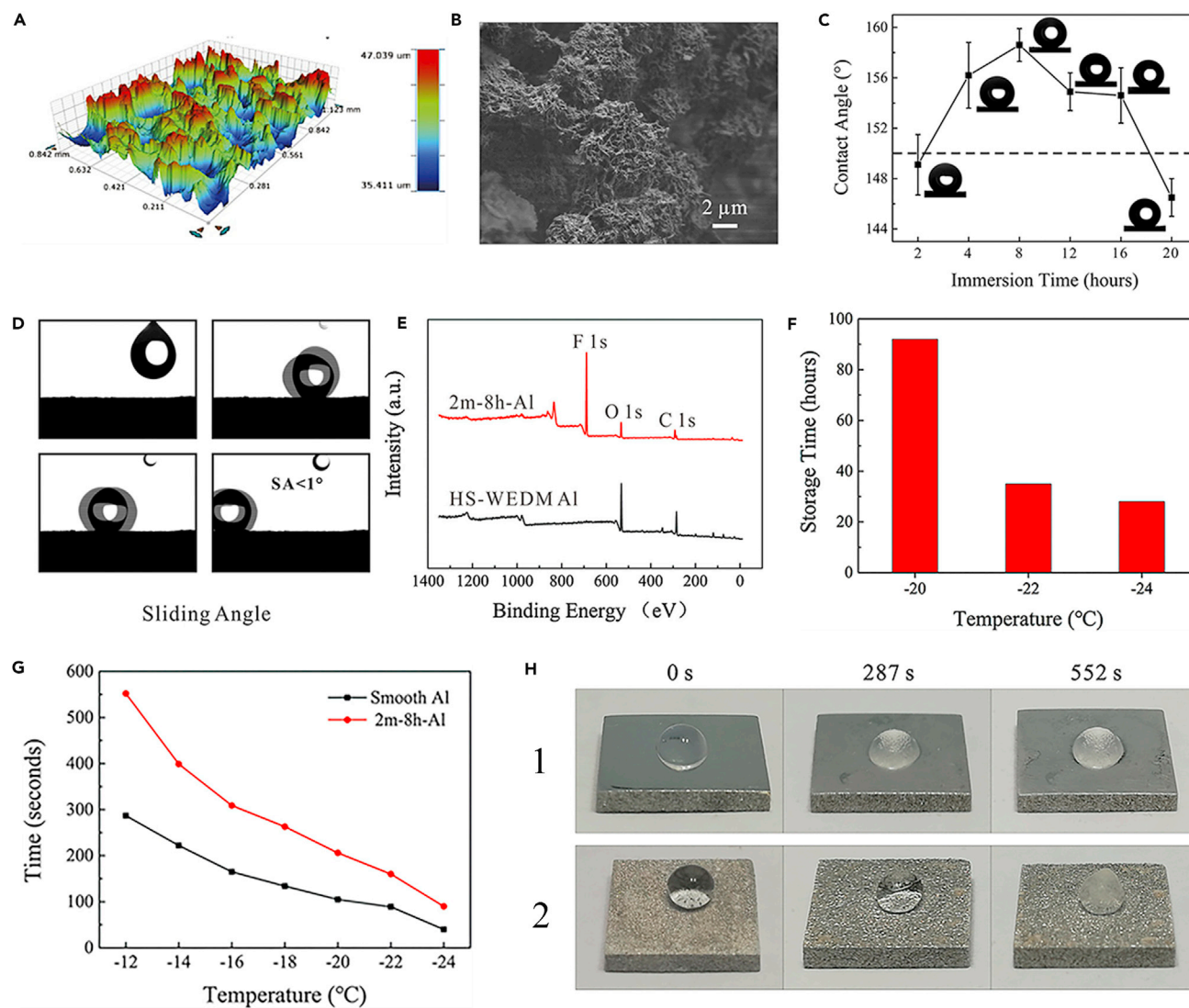
Figure 15. Study on SH and anti-icing properties of SH aluminum alloy samples

(A) The cut aluminum alloy sample was etched with hydrochloric acid solution, and the white light interferogram after etching for two minutes was shown.

(B) Scanning electron microscope image of an aluminum alloy specimen etched for two minutes and immersed in perfluorooctanoic acid (PFOA) solution for eight hours.

(C) The CA curves of SH aluminum alloy at different soaking times; the illustration shows an optical image of a static water drop.

(D) Shows the SA of an SH aluminum alloy soaked for 8 h.

(E) XPS spectra of SH aluminum alloys.

(F) The average freezing delay time of smooth and SH aluminum alloy samples varies with temperature from −12°C to −24°C.

(G) Low temperature durability of SH aluminum alloy samples at −20°C to −24°C.

(H) The digital images of water droplet freezing process of smooth aluminum alloy samples (1) and SH aluminum alloy samples (2) with different time at −12°C are presented. Image reprinted with permission from Sun et al. (2020a).

gradually with the decrease of temperature. It can be seen intuitively in Figures 15G and 15H; the average freezing time of water droplets on the smooth aluminum alloy surface drops from 287 to 40 s. In addition, on the surface of SH aluminum alloy sample, the average freezing time of water droplets also has the same trend. The average freezing time decreased from 552 to 90 s. That is almost twice as much as smooth aluminum. According to the Cassie-Baxter state (Cassie and Baxter, 1944), SH aluminum alloy has an air layer between the surface microstructure and the water droplets (Villeneuve et al., 2019), and the water droplets remain spherical before and after freezing. Tang et al. (Tang et al., 2015) found that the surface thermal conductivity is related to the contact area of the water droplets on the aluminum

alloy surface. With small contact area and slow thermal conductivity, SH aluminum alloy has better anti-icing performance.

In addition, according to the Figure 15F, it can be found that the SH aluminum alloy has excellent low temperature durability, which also guarantees its SH performance and anti-icing performance.

Compared with the hydrophilic surface, the condensate droplets in the Cassie-Baxter state (Cassie and Baxter, 1944) on the SHS have greater heat transfer resistance and smaller contact area on the under-cooled surface. At the same time, the total heat loss of the droplet on the SHS is less than that on the hydrophilic surface, which prolongs the freezing initiation time. The freezing delay is related not only to the higher hydrophobicity and the lower solid-liquid contact area of the condensate droplets but also related to the higher ice nuclear barrier (Qiu et al., 2019). In addition, Shen et al. (2015a) proved that the SHS has a certain anti-icing performance by analyzing the nucleation rate and the total nucleation rate of the solid-liquid interface on the three different surfaces. From the flat substrate surface to the SH nanostructure surface, the nucleation rate at the solid-liquid interface decreases gradually, and the nucleation rate at the solid-liquid interface caused by the nano-conical structure is smaller than that of the lamellar nano-porous structure. In addition, some scholars used to add nucleation inhibitors to improve the anti-icing performance of SHS. For example, Guo et al. (2019) used nucleation inhibitor polyvinyl alcohol (PVA) to improve the prepared SH POSS/PDMS coating, so as to improve its anti-icing performance (as shown in Figure 16A). Although PVA is hydrophilic, the surface wettability of the SH POSS/PDMS coating can be determined by the morphology of the SH POSS/PDMS coating. Through the observation of the scanning electron microscope (Figure 16B), the morphology of PVA-POSS/PDMS coating is basically similar to that of POSS/PDMS coating. And in Figure 16C, the CA is about 150°, indicating that the PVA-POSS/PDMS coating has good water resistance. Under appropriate conditions (particle spacing is less than 8.82 μm), the solidification temperature of water droplets on the SH coating decreases by about 2°C (as shown in Figure 16D). This is because the hollow microspheres make the droplets become Cassie-Baxter state (Cassie and Baxter, 1944), reducing the contact area between the droplets and substrate and the microspheres between the hollow microspheres or entering the hollow hinder heat conduction. At the same time, PVA coating covers some nonhomogeneous nuclear points on the surface of micro and nano structures, so that the hydroxyl group in PVA can form hydrogen bonds with water molecules, which destroys the arrangement of water molecules at the interface, affects the freezing process of water, and ultimately reduces the freezing temperature (Wu et al., 2019a). However, when the particle spacing is greater than 8.82 μm, the water droplets on the surface will no longer be in the Cassie-Baxter state (Cassie and Baxter, 1944; Qi et al., 2020c), and the hydrophilic PVA will increase the contact area between the surface and water, resulting in the increase of freezing temperature of the water droplets. The results show that the nucleating agent has synergistic anti-icing effect with SH micro-nano structure surface under the best matching conditions.

In terms of total ice core rate, the SH nanostructure also decreased significantly compared with the flat substrate surface. This is because the layered molecular film with low surface free energy and the constructed microstructure increase the energy barrier of the ice core. However, there is no difference in the total ice rate between the two SH nanostructures, because the nucleation rate of the body ice is dominant, which is much higher than the ice formation rate at the solid-liquid and liquid-gas interfaces. Therefore, compared with the flat substrate surface, the SH nanostructure surface can greatly reduce the nucleation rate at the solid-liquid interface due to its extremely low actual solid-liquid contact area and special contact type (Pan et al., 2019). The nano-cones contact with the droplets in a "point contact" manner, which leads to a lower nucleation rate of solid-liquid ice (Shen et al., 2019c). It has been reported that the ice on the SHS has a lower macroscopic growth rate due to the low nucleation rate of the ice and the insulating effect of the air bag on the SHS. At the same time, combined with the classical nucleation theory, the SHS can greatly reduce the nucleation rate at the solid-liquid interface (Shen et al., 2015a).

What is noteworthy is that the extension of freezing time of SH materials is affected by many factors, such as nucleation rate of solid-liquid interface, surface wetting state, temperature, and surface microstructure. Moreover, these factors are mutually contained and affect each other, which often leads to some complex and difficult to explain results. However, compared with the bare surface, the surface using the SH material does extend the freezing time. So far, a large number of studies have shown that SHS can only delay the
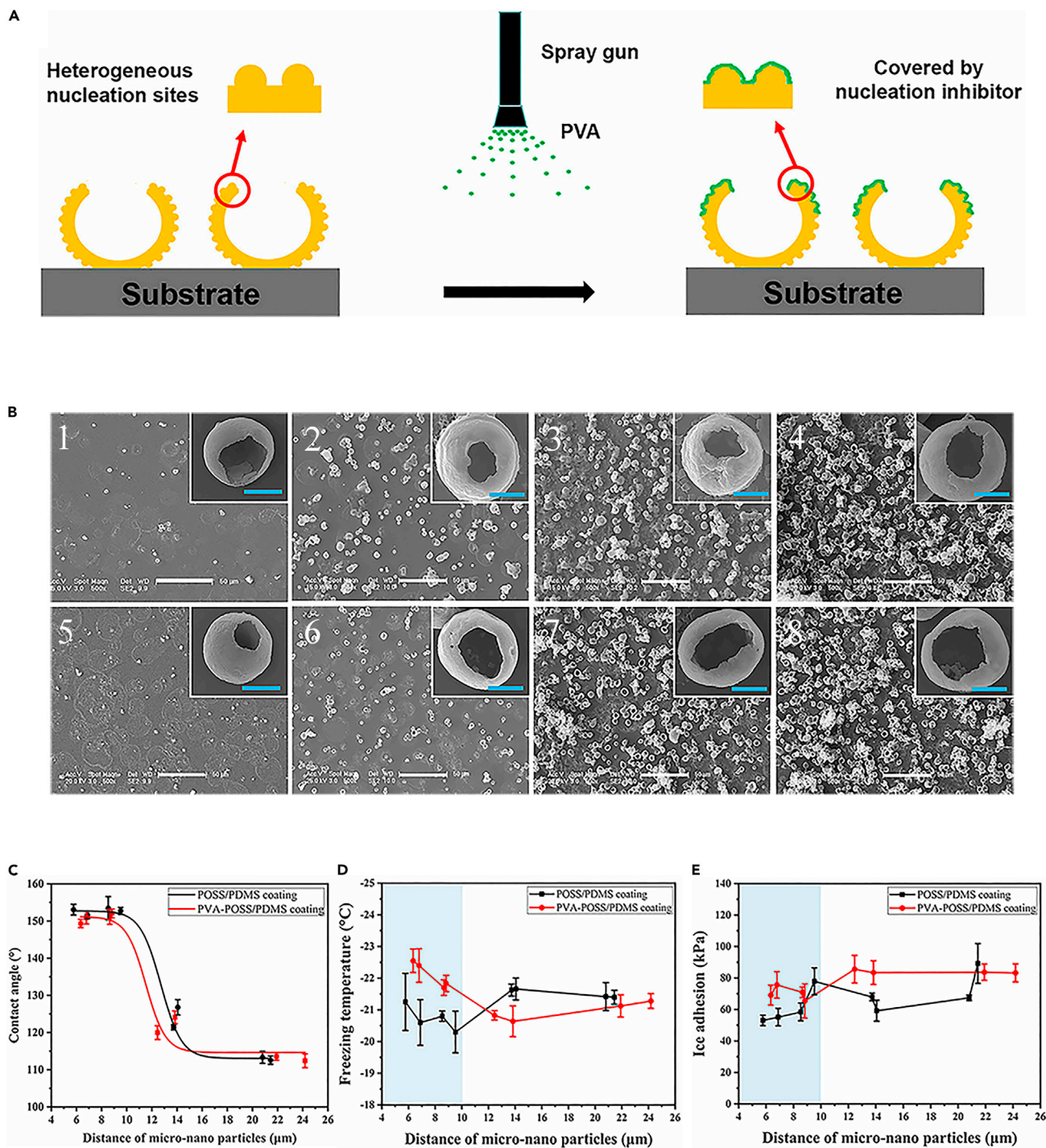
Figure 16. Study on the improvement of anti-icing performance of SHS by nucleating corrosion inhibitor

(A) Illustration shows the synergism of nucleation inhibitor and hydrophobic micro-nano structures.

(B) Typical PVA-POSS/PDMS coatings and POSS/PDMS coating with particle distance of 21.91, 13.83, 8.82, and 6.34 μm.

(C–E) Anti-icing performances of PVA-POSS/PDMS coatings with different particle distances: (C) CA, (D) freezing temperature of droplet, and (E) ice adhesion. Image reprinted with permission from Guo et al. (2019).

time of surface icing but cannot completely inhibit the surface icing phenomenon. Especially in some extreme environments (such as high humidity environment, cold condensation frost, etc.), freezing of SHS is inevitable. Studies have shown that on SHSs, although ice may freeze, the adhesion of the ice to the surface should be so low that the ice on the surface can be easily removed by external forces such as gravity, aerodynamics, or rocking forces (Li and Guo, 2018).

REDUCING THE ADHESION OF ICE

Ice adhesion is one of most significant parameters for evaluating the anti-icing properties (Zheng et al., 2020). It gives us an indication that the ice that forms on the surface can be easily removed. The strong adhesion of ice on the surface of solid materials is largely attributed to the strong interaction between polar ice molecules and solid molecules, which is usually caused by the interaction of hydrogen bonds, van der Waals forces, and electrostatic interactions. It should be noted that the aforementioned is the main physical mechanism of ice adhesion on the surface (Jia et al., 2020; Zhang et al., 2019a). Among them, many researchers believe that direct electrostatic interaction is the main factor (Richard et al., 2002). In order to reduce the direct contact between ice and solid, it is necessary to reduce the direct electrostatic interaction between ice molecules and solid molecules. In the study of SH materials, it is found that SH materials can significantly reduce the adhesion between surface water droplets or ice coating and itself. With the increase of CA, the adhesion between surface ice coating and solid surface will be lower (Golovin and Tuteja, 2017; Zhang et al., 2019a). Tang et al. (2020) found that with the increase of surface roughness, the ice adhesion force firstly decreased and then increased sharply. Among them, the surface with moderate surface roughness produces lower ice adhesion (Nguyen et al., 2019), which is mainly attributed to the lubrication of the SH layer. Due to the smaller nanoscale roughness, the condensate on the SHS is often too cold, thus preventing the formation of the ice meniscus below $-20°C$, resulting in lower ice adhesion. Although, according to the Cassie model (Cassie and Baxter, 1944), higher surface roughness can effectively reduce the actual contact area and improve the hydrophobicity. However, for the freezing process in the atmosphere with limited humidity, condensation will occur, and the water meniscus will form between the roughness of water droplets and the SHS. Finally, the ice surface will form, and the mechanical linkage between the ice and the surface roughness will form, leading to the decline of the ice abhorrence (Chen et al., 2012). In his freezing experiments, Feng et al. (2018) found that the trapped air on the surface of the SH aluminum alloy not only keeps the water droplets on top of the convex region but also reduces the actual contact area between the ice and the coating surface, reducing the mechanical anchoring effect. Therefore, when the surface freezes, it usually forms loose ice. Moreover, the volume of water increases after freezing, which compacts the trapped air on the SHS, resulting in a reaction force. It can reduce the adhesion between the ice and the SH aluminum alloy surface. At the same time, Nguyen et al. (2018) also found that the contact area between actual ice and SHS plays an important role in reducing ice adhesion. Because the contact area is reduced, heat transfer, mainly through nanotubes, is reduced, and the interaction of ice droplets with the substrate in their freezing form is prevented, reducing adhesion (Nguyen et al., 2018). However, some researchers have found that the surface with micro and nano structures can not only encapsulate gas to induce superhydrophobicity but also provide sites for accelerating heterogeneous nucleation (Shen et al., 2015a). Microstructure of the surface improves the anchoring effect, resulting in a much stronger adhesion of the surface ice (Cui et al., 2019; Shen et al., 2019c; Tong et al., 2019). So far, it has been controversial whether SHSs can reduce the adhesion of ice. Although the bonding strength of ice on a surface can be characterized by shear or tensile bonding tests, there is no standard test for ice adhesion, and most research groups have their own testing equipment (Shen et al., 2019a).

THE PRACTICAL APPLICATIONS

It is concluded that the SHS has certain anti-icing performance from many aspects, from the timely removal of water droplets on the surface before freezing, to the improvement of the anti-icing performance of the SHS by delaying the freezing time, and the reduction of the ice adhesion on the surface. In fact, the ultimate purpose of the research on SH materials is to hope that they can be used in real life to benefit ourselves. In this section, it will briefly introduce the applications of some SH materials in anti-icing.

First of all, SH materials can be applied to the heat exchanger of air conditioning. Through chemical oxidation and subsequent chemical modification, Wang et al. (2018) manufactured the finned tube heat exchanger of SH air conditioning with dew-jumping effect (as show in Figure 17A). Combined with the typical FESEM images of the nanoarray in Figures 17B–17D, the static CA of 5 μL water droplets on the surface of the foil is $162 \pm 2.4°$ and the rolling angle is $3.5 \pm 0.2°$, indicating that this nanoarray foil is SH. The

A Etching → Boiling → Fluorinating

B

C

D

E

F

G
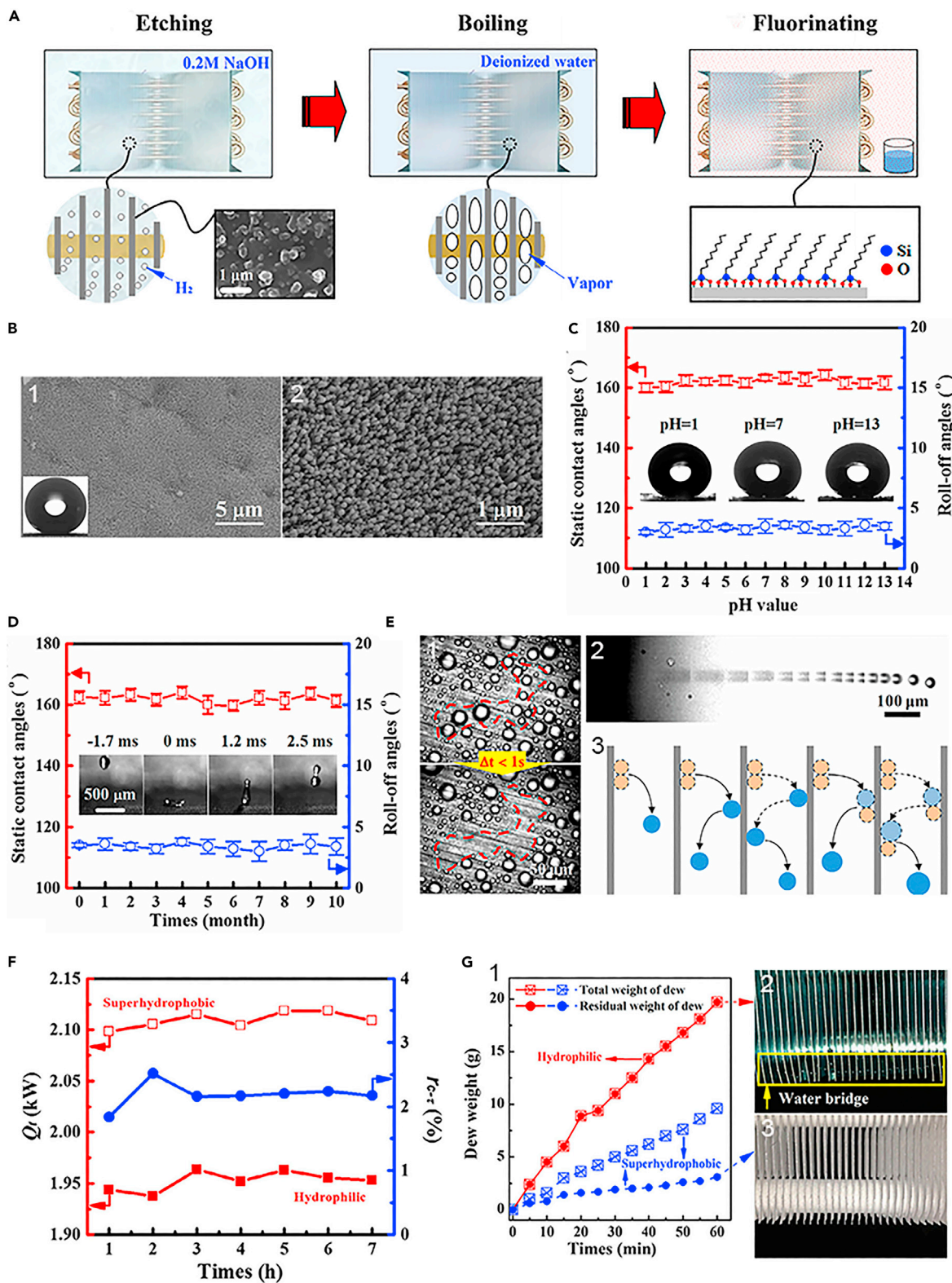
Figure 17. A novel air-conditioner fin-tube heat exchanger with SH foils

(A) Schematic illustration of the method to fabricate the novel heat exchanger having SH aluminium foils. (1) Etching to remove oxides and activate and roughen the foil surface. (2) Boiling in deionized water to create $Al(OH)_3$ nano-arrays. (3) Fluorinating to obtain a layer of fluorosilane on the texture to form superhydrophobicity.

(B) FESEM images with (1) low and (2) high rate of the nano-arrays on the SH foil. Inset of (1): the static CAs on an SH foil.

(C) SCAs and RAs of water droplets with different pH values on the foil. Inset of (C): optical image of the water SCAs with pH = 1, 7, 13.

(D) SCAs and RAs on the foil change with month. Inset of (D): time-resolved images of the bouncing of a diameter of ~150 μm drop on the superamphiphobic foil.

(E) Superhydrophobicity and condensation behavior of the SH aluminum foils. (1) Time lapse images of condensation captured via a high speed camera, showing a self-jumping behavior of several drops on a horizontally placed foil from the top view. (2) The self-jumping movement track of a dewdrop with a diameter of ~30 μm demonstrated by an overlapped optical image on a vertically placed foil. (3) Schematic illustration of five possible modes of the jumping drops keeping the fins always dry.

(F) The relationship between total cooling capacity and RC-growth index and time.

(G) Condensation characteristics of an SH heat exchanger. (1) Change in dew weight recorded every 5 min. Optical magnification of (2) hydrophilic and (3) SH heat exchanger bottom after 1 h condensation. Image reprinted with permission from Wang et al. (2018).

nanoarray foil made from a treated heat exchanger can remain SH in water at different pH levels and can even be exposed to the natural environment for up to 10 months. As can be seen in Figure 17E (1), more than 10 droplets changed their positions within less than 1 s. Combined with the jumping droplets observed on the surface of the vertically placed foil in Figure 17E (2), it can be seen that more than 10 droplets should quickly merge on the surface and leave through jumping movement. Moreover, Wang et al. predicted five types of jump trajectories (Miljkovic et al., 2014) as shown in Figure 17E (3): (1) two droplets merge and jump out; (2) the combined droplet rebounds and jumps out; (3) the combined droplet bounces back multiple times and jumps out; (4) the merged droplet is triggered by the kinetic dew and jumps out; (5) the merged droplet jumps out after multiple triggering (Peng et al., 2020). As can be seen from the Figure 17F, the total dew weight of the hydrophilic heat exchanger is twice as much as that of the SH heat exchanger, so the continuous jumping behavior with excellent anti-condensation effect can be maintained. In addition, the dew weight remaining on the hydrophilic heat exchanger is five times as much as that on the hydrophilic heat exchanger after one hour. Compared with conventional hydrophilic exchangers, the SH exchangers also gain more than 8% and 2% cooling capacity and heat transfer coefficient under rated output conditions. Moreover, the SH outdoor condenser under frosting condition has a higher energy conversion rate (more than 85%) after 60 min than the conventional hydrophilic condenser. Figure 17F shows the comparison of cooling capacity between the hydrophilic exchanger and the SH exchanger. It can be seen that the condensation heat transfer performance of the SH exchanger is significantly higher than that of the traditional hydrophilic exchanger (Wang et al., 2018).

Figure 17G (1) on the right describes the change of total and residual moisture over time on hydrophilic and SH heat exchangers. By comparison, it is found that the total amount of dew on the SH heat exchanger is less. It was further found that the hydrophilic heat exchanger in Figure 17G (2) formed a water bridge at the bottom, whereas the SH heat exchanger did not have obvious dew drops (see Figure 17G (3)). It is well known that the appearance of dew on the aluminum foil of heat exchanger will reduce the condensation efficiency of the heat exchanger. The SH aluminum foil has good anticoagulant effect, greatly improving the condensation efficiency of heat exchanger, which has self-cleaning, mildew resistance, and other properties, prolonging the service life.

SH materials are also reported to be used in road construction. Nowadays, in road construction, asphalt is used to lay the road surface. However, icing on asphalt pavement will affect not only the road surface structure but also affect driving safety. In order to improve asphalt road, Peng et al. (2020) prepared acrylic SH coating (ASC) for asphalt road by using acrylic coating and carbon nanotubes as raw materials. By comparing Figure 18 A and B, the water droplets appear spherical on the surface of ASC. The CA of water droplet on the slag concrete surface is 155.173°, and the rolling angle is 4.26° (as show in Figure 18B). The ASC can reduce the contact area between the water droplets and the surface, so that the water droplets are separated from the surface at a small inclination angle. As show in Figure 18C, it can be seen that when water drops on the road, the water drops will automatically fall into the ditches on both sides of the road. In addition, the carbon nanotubes formed micro-nano rough structure on the surface of ASC, which improved the friction coefficient of the road surface and had a certain anti-skid performance. By measuring the permeability coefficient of asphalt mixture samples, the cylinder water level of acrylic acid coating (AAC) asphalt pavement and the ASC asphalt pavement can remain unchanged for 3 min, indicating that both of them have good waterproof performance. In addition, as shown in Figure 18E (1), the water
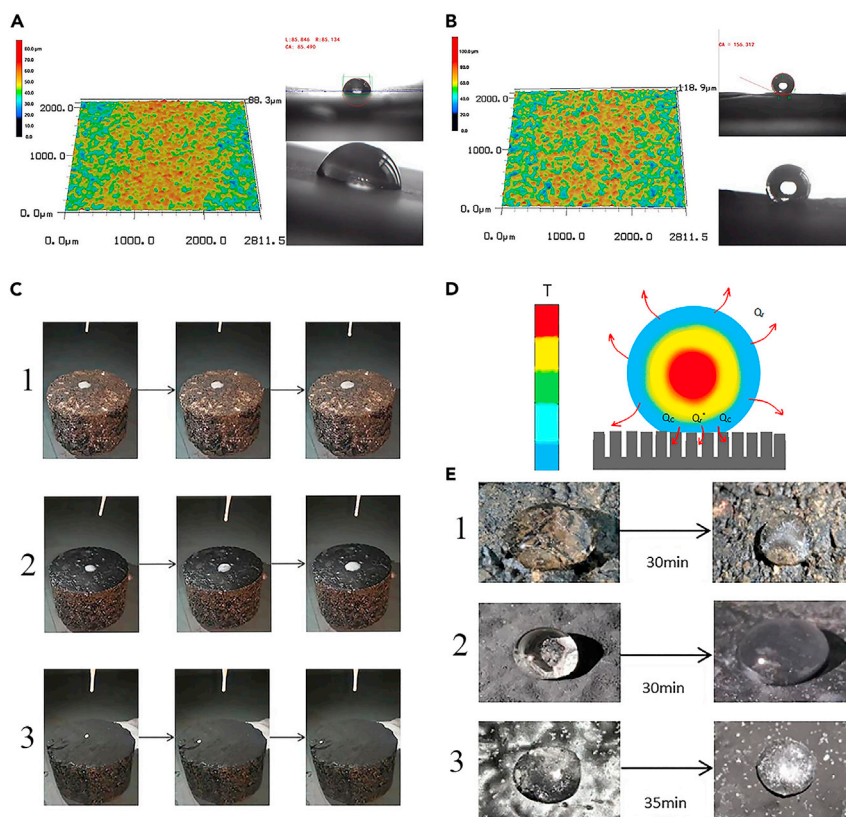
Figure 18. Investigation of anti-icing, anti-skid, and water impermeability performances of an acrylic SH coating on asphalt pavement

(A) 3D topographic image, CA testing photo, and rolling angle testing photo of AAC.

(B) 3D topographic image, CA testing photo, and rolling angle testing photo of ASC.

(C) (1) Photos of a water droplet on the asphalt mixture surface; (2) photos of a water droplet on the AAC-coated asphalt mixture; (3) photos of a water droplet on the ASC-coated asphalt mixture.

(D) Schematic the heat transfer diagram of a water droplet on an ASC.

(E) (1) Photos of a water droplet on the asphalt mixture before and after freezing; (2) photos of a water droplet on the ACC-coated asphalt mixture before and after freezing; (3) photos of a water droplet on the ASC-coated asphalt mixture before and after freezing. Image reprinted with permission from Peng et al. (2020).

droplets on the surface of the asphalt mixture become opaque and solidify after freezing for 30 min. In Figure 18E (2), the surface of AAC-coated asphalt mixture appears the same state as Figure 18E (1) after freezing for 30 min, indicating that the two asphalt mixtures in Figure 18E (1) and Figure 18E (2) have the same ice resistance. However, in Figure 18E (3), the water droplets on the surface freeze after 35 min. Through comparison, it is obvious that the ASC can delay the time of surface icing, which proves that the ASC has certain anti-icing performance and can indeed improve road safety (Peng et al., 2020).

In addition, SH materials can also be used in communication and transmission lines, aircraft, and other fields to prevent disasters caused by surface ice. However, in the process of industrialization, besides the durability of SHS, the complexity and cost of process must also be considered (Balordi et al., 2019; Liu et al., 2020b). The complexity of the process and the high cost of raw materials greatly limit their widespread production at the industrial level.

Existing problems

Although, SH coatings with the WCA >150° and the SA < 10° have been widely reported to resist water droplet adhesion and inhibit icing. However, it should be noted that the structures of SH materials are all convex cylinders on the micro and nano scale, which not only provide suitable traps for air bags but also significantly reduce the interaction between ice and the anti-icing surface (Khanmohammadi Chenab,

2020). With the extension of the use of time, the micro- and nano-scale columns have a smaller diameter, brittle texture, and are easily broken by external forces, destroying the surface's superhydrophobicity. In addition, when the wetting state of the SHS changes, that is, when the surface is Wenzel-type (Zhang et al., 2018), the water droplets will penetrate into the cavity with rough surface, and cannot slip off, which will remain in the nailed state. At this point, once the water droplets freeze, the surface structure will be destroyed, resulting in the ice surface contact area and ice adhesion strength, so that the superhydrophobicity loss, unable to ice-proof. On the other hand, poor particle-substrate interface interaction on the SHS, long operation under load, and multi-peak roughness may also lead to brittle mechanical stability of the coating (Jing and Guo, 2018; Li and Guo, 2018). In addition, in order to obtain SH nanocomposite coatings on the surface of lotus leaves, many researchers use various inorganic fillers such as ZnO (Zhou et al., 2019a), TiO_2(Zhou et al., 2019b), Al_2O_3 (Lee et al., 2018b), and other nanoparticles (Li et al., 2019c) to construct layered rough structures. This creates an SH structure, but these metal oxides are vulnerable to corrosion and wear when used in harsh conditions such as acidic solutions, which leads to the integrity of the coating and the loss of superhydrophobicity (Wu et al., 2020).

However, it remains a huge challenge to synthesize a coating that can be applied to any surface and function effectively. More importantly, the coating should be strong enough to withstand repeated icing or frosting in practical applications (Bai and Zhang, 2019).

The latest development

In recent years, with the continuous development of SH materials, researchers have studied many methods to solve the problem of poor mechanical stability of SHS for anti-icing, such as the combination of passive anti-icing and active de-icing to improve the anti-icing performance of the substrate surface (Hu and Jiang, 2020; Wang et al., 2020c). For example, Wang et al. (2020c) proposed an SHS and electrothermal anti-icing method based on graphene composites. It is well known that carbon nanomaterials are typical hydrophobic materials with low surface energy (SE) (Baldelli et al., 2020; Taherian et al., 2013). SEs of CNTs could be at the range of 27–45.3 mJ/m^2 (Roh et al., 2014). SEs of chemically exfoliated graphene and graphene oxide (GO) have shown to be 46.7 and 62.1 mJ/m^2, in that order, whereas that of normal graphite flake was ~54.8 mJ/m^2 (Wang et al., 2009b). As a member of carbon nanostructures and their composites, graphene has attracted extensive attention due to its high specific surface area, excellent electrical conductivity, excellent thermal conductivity, and excellent mechanical strength (Geim, 2009; Saji, 2021). Jiang et al. recently bonded the double-scale TiO_2 nanoparticles with the binder to produce a durable SHS with a maximum wear distance of 8.00 m under a 100 g load (Jiang et al., 2018). Inspired by this work, Wang et al. (2020c) constructed a hierarchical structure using the three-scale characteristics of inorganic fillers (graphene, carbon nanotubes, and silica nanoparticles) in order to improve the durability of SHS. The fractional structure is then embedded into the bottom by simple dissolution and recrystallization. The synergistic effect of this graded roughness, partial inset structure, and graphene provides excellent wear resistance to 500 g loads, 8.00 m sandpaper wear, various corrosive fluids, and low/high temperature treatments without loss of superhydrophobicity. Below 0°C, graphene composites are SH, which can delay the freezing time of supercooled water. The water droplets on the exposed glass are hemispheric and completely frozen after 57 s. On the surface of the SH graphene sample, there is an almost spherical water droplet, and the delayed freezing time is 335 s. Even after the complete freezing, the water droplet remains spherical. And under simulated "ice glaze" conditions, although ice forms on the surface when the DC voltage is turned off, the ice thickness is about 3 mm. However, the superhydrophobicity can still be observed after 70 s rapid de-icing under 50 V voltage without water droplet retention. In particular, this SH graphene composite retained de-icing property even after 30 icing/de-icing cycles (Wang et al., 2020c).

What is more, Sun et al. (2020b) has developed a controllable integrated electric heater for aerospace applications based on a super-flexible CNW/PDMS bionic SH nanocomposite. Two kinds of anti-icing strategies for biomimetic nanocomposites were proposed. One is passive anti-icing strategy. The static WCA of passive anti-icing line is 155.4 ± 0.5°, and the moving deionized water droplets can roll off the biomimetic surface before freezing. To condense on the surface of the water droplets in high humidity (RH = 85%) and freezing point temperature environment (about −5°C), it reduced the heat transfer efficiency of the substrate and reduced many of the available nucleation sites. It means that the water droplets on the surface of the freeze behavior was delayed. However, the passive anti-icing behavior of the bionic SHS cannot completely prevent icing for a long time. Once the first layer of ice is formed, the passive defences are completely lost. Therefore, it is necessary to establish a second defense line of

active electrothermal de-icing in order to eliminate any icing phenomenon on the surface of nanocomposites. The bionic nanocomposite film was transformed into an electrothermal active de-icing defense line as applied voltage. The biomimetic nanocomposite has excellent thermal stability and reliability. The columnar texture remains intact during repeated icing/de-icing cycles. The results show that the SH nanocomposites have excellent passive anti-icing performance and active electrothermal de-icing performance (Sun et al., 2020b). Although these composites are promising de-icing candidates, practical anti-icing/de-icing and damage-resistance properties face challenges in large-scale applications (Zhao et al., 2018).

To date, three main techniques have been developed to improve the mechanical stability of SH materials: (1) doping some flexible polymer substrates to improve the mechanical stability of SHS coatings, such as acrylic resin (Dong et al., 2019), polydimethylsiloxane (PDMS) (Liu et al., 2017), silicone adhesives (Li et al., 2016), polyurethane (PU) (Lv et al., 2020), and epoxy resin (Liu et al., 2019b). The introduction of these polymer substrates can not only play a role in adhesion, improving the adhesion between nanoparticles and matrix, but also contribute to anti-wear and scratch energy dissipation, improving the mechanical durability of SH coating (Shen et al., 2019b; Zhang et al., 2019b). In addition, from the point of view of materials, such as PDMS (Liu et al., 2017), SH coating has excellent chemical stability, good wear resistance, excellent hydrophobicity, and strong adhesion to the substrate, so it is a common use of non-fluoropolymer binder for the construction of SH coatings (Ge et al., 2020).

For example, Bai and Zhang (2019) used a simple self-assembly technique to prepare a new coating in the aluminum surface (as show in Figure 19A). It is a fluorine base graphene oxide (GO)- diatomaceous earth (DE)/epoxy (EP) composite coating, which has low surface energy microstructure. According to the SEM image in the Figure 19B (1), the microstructure characteristics of GO-DE particles provide a high specific surface area for EP curing, thus forming GO-DE/EP ternary composite. It can be seen from Figure 19B (2) that EP plays an important role in the structural stability of the composite coating, which makes the surface of the coating have rough morphology. The WCA of the composite coating is 161.3 ± 2°, and the SA is 5.8 ± 1.2°. In addition, the composite coating can be constructed on cloth, paper, and latex glove substrates and has good SH property (as show in Figure 19F). During the evolution of water droplets on the coating surface in Figure 19C, due to the layered structure of the coating surface, the contact area between the water droplets and the surface becomes small. The composite particles let the air trapped in the gap, resulting in the heat transfer between droplets and coating. Through the contrast it can be found that the composite coating can extend surface water droplet's freeze time. After the abrasion tests, the abraded coating still exhibits better inhibition of ice growth. Besides, the GO sheets in the coating are attached to the ice embryo through hydrogen bonding, the curve of ice crystals formed between the GO sheets. By Kelvin effect, it had depressed the frozen temperature and inhibited the growth of ice crystals. Cohesive force of the EP is stronger, so it cannot be stripped. In addition, the coating maintains complete SH and anti-icing performance after the 50-cycle sandpaper abrasion (Figures 19D and 19E) (Bai and Zhang, 2019). For another example, Qi et al. (2020a) prepared a new SHS based on nano-silica assembly by exposing commercial nano-silica modified with n-octyltriethoxysilane to the surface and attaching it to the substrate through a polymer epoxy resin. It has excellent superhydrophobicity and ultra-small SA, prolonging the formation time of ice core on the surface and has good ice resistance at ultra-low temperature. Owing to the polymer attached to the surface, it shows good mechanical stability (Qi et al., 2020a).

In addition, the other two techniques are as follows: (2) applying a microscale "shell" to protect the nanostructures that provided water repellency (Wang et al., 2021b). It can form a rigid SHS on metal, glass, and silicon substrates, which can prevent nanostructures from being removed by larger size abrasives, maintain good SH properties even after sandpaper and a sharp blade wear (Wang et al., 2020a). This is shown in Figure 15A. (3) Using hydrophobic nanoparticles to fabricate free-standing particle-polymer composites (Wang et al., 2021b). When the SHS is worn away or removed, a new layer of SHS will be formed (Enomoto et al., 2018). In this way, it can greatly extend the use time of SH materials. In fact, three techniques are often combined with each other in the study of superhydrophobicity.

Although these composite SH materials are promising de-icing candidates, practical anti-icing/de-icing and anti-damage properties in large-scale applications face challenges. Therefore, in order to improve the application of SH materials in real life, further research and development are needed.
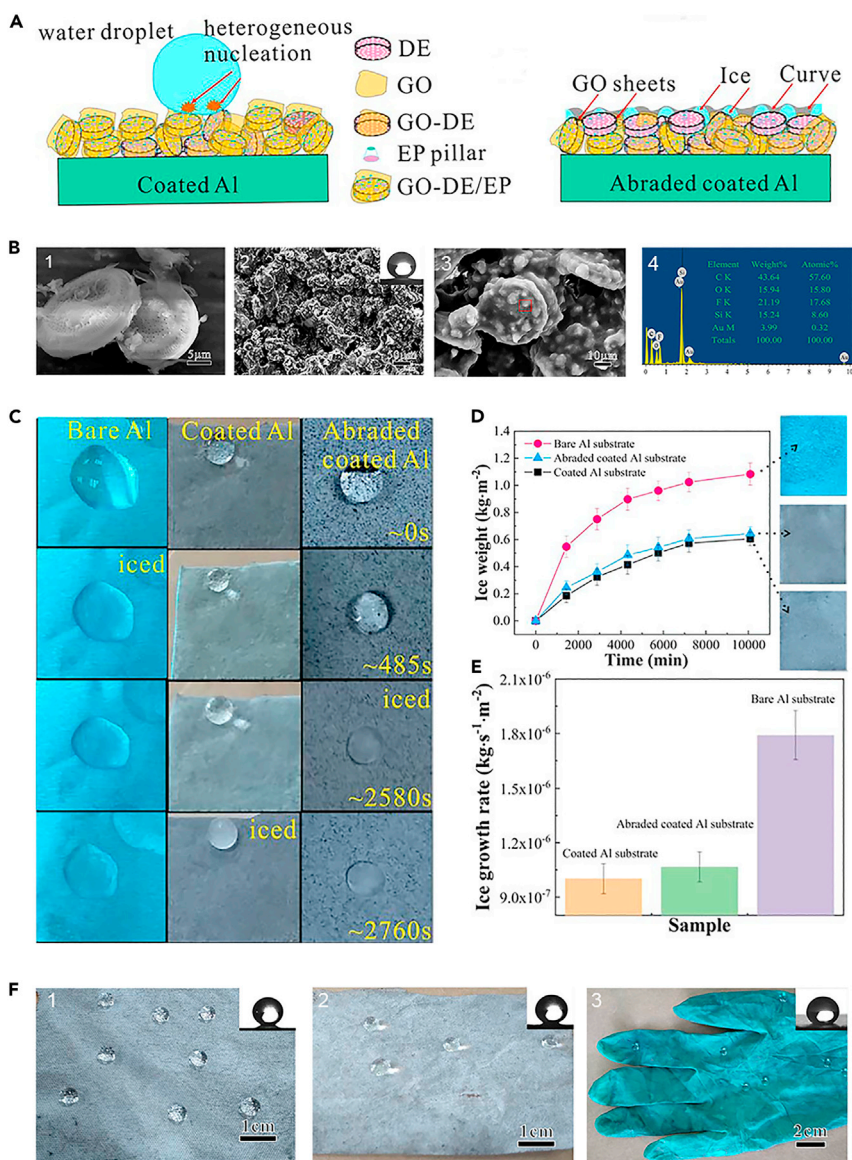
Figure 19. Study on mechanical stability of anti-icing graphene oxide diatomite/epoxy coatings
(A) Schematic illustrations of heterogeneous nucleation mechanism of a water droplet on coating surface and freezing-inhibited mechanism of GO sheets.
(B) SEM images of GO-DE particles: (1) SH GO-DE/EP composite coating on Al surfaces at (2) low and (3) high magnifications. (4) EDS spectrum of specimens.
(C) Photographs of icing time of specimens.
(D) Change of ice weight with time.
(E) Ice growth rate of freezing for different specimens.
(F) Photographs of SH GO-DE/EP coating fabricated on (1) cloth, (2) paper, and (3) latex glove substrates. Image reprinted with permission from Bai and Zhang (2019).

CONCLUSIONS

It is found that the SHS can increase the free energy barrier of ice core and reduce the heat transfer between the droplet and the surface because of its lower surface energy and smaller droplet contact area. Therefore, surface icing can be controlled to some extent by rational use of SHS with micro/nano or hierarchical surface structure and low surface energy chemical composition. In this review, the research progress of SH materials for anti-icing in recent years has been introduced from the beginning. Next, the mechanism of solid

surface icing and two classical nucleation theories are also outlined, which provide theoretical support for adjusting ice formation of solid surface and designing passive anti-icing surface.

Compared with the active de-icing method, the SHS can realize passive anti-icing by timely cleaning of water droplets on the surface before freezing, delaying the freezing time, and reducing the adhesion force of ice on the surface. Before water droplets are frozen on the surface, the SHS has a certain self-cleaning function for droplets colliding and condensing on the surface due to the large WCA and the small SA. However, in the high humidity environment, the water droplets on the SHS are always present and cannot be completely removed. In addition, when water droplets freeze on the surface, the SHS can delay the freezing time to prevent ice due to its special micro-nano structure. The micro-nano or layered structure of the SHS can capture the air to form an air bag, thus reducing the heat transfer between the water droplets and the substrate to prolong the freezing time. In addition, the nucleation rate of surface ice nuclei can be reduced by adding nucleation inhibitors to the SHS. When ice inevitably forms on the surface, it has been reported that SHSs can reduce the adhesion of ice to the surface, whereas it has also been suspected that SHSs can increase the anchoring effect of ice on the surface. Further research is needed to confirm this. From a practical point of view, SH materials with good mechanical stability are desirable in anti-icing. For example, grafting the polymer epoxy resin on the SHS not only improves the mechanical stability of the material (Zhang et al., 2019b) but also has excellent anti-icing performance.

It is well known that the surface morphology of SHS will directly affect its performance, as well as the nucleation and crystallization of ice on the surface. On this basis, ordered rough structures, appropriate micro/nano microstructure, and SHSs with high mechanical strength can be constructed on the surface. At present, multi-functional SHSs with self-repair, self-migration, self-healing, and other characteristics can self-repair and even regenerate after wear, which greatly improves the service life of SH materials and brings hope that SH materials can be widely used from the laboratory to practical life.

However, in the current research progress, part of the preparation method is expensive, complex process and is not suitable for large-scale production and application, so there is a great space for development in structural optimization and material selection. From my personal point of view, future research by researchers should focus on preparing surfaces with methods that are easy to operate, low-cost, environmentally friendly, and durable. Finding new solutions to ice is also crucial. Finally, I always believe that there will be more breakthrough work done by researchers in the near future. The practical application of SH materials in daily life and industrial fields will be further improved.

AUTHOR CONTRIBUTIONS

H.H. conceived and designed the project and wrote the manuscript. Z.G. conducted the instruction.

DECLARATION OF INTERESTS

The authors declare no competing interests.

REFERENCES

Azimi Yancheshme, A., Allahdini, A., Maghsoudi, K., Jafari, R., and Momen, G. (2020). Potential anti-icing applications of encapsulated phase change material–embedded coatings; a review. J. Energy Storage 31. https://doi.org/10.1016/j.est.2020.101638.

Bai, Z.-G., and Zhang, B. (2019). Fabrication of a mechanically-stable anti-icing graphene oxide-diatomaceous earth/epoxy coating. Mater. Res. Express 6. https://doi.org/10.1088/2053-1591/ab2321.

Bai, G., Gao, D., Liu, Z., Zhou, X., and Wang, J. (2019). Probing the critical nucleus size for ice formation with graphene oxide nanosheets.

Nature 576, 437–441. https://doi.org/10.1038/s41586-019-1827-6.

Baldelli, A., Ou, J., Li, W., and Amirfazli, A. (2020). Spray-on nanocomposite coatings: wettability and conductivity. Langmuir 36, 11393–11410. https://doi.org/10.1021/acs.langmuir.0c01020.

Balordi, M., Cammi, A., Santucci de Magistris, G., and Chemelli, C. (2019). Role of micrometric roughness on anti-ice properties and durability of hierarchical super-hydrophobic aluminum surfaces. Surf. Coat. Technol. 374, 549–556. https://doi.org/10.1016/j.surfcoat.2019.06.001.

Barthlott, W., and Neinhuis, C. (1997). Purity of the sacred lotus, or escape from contamination in biological surfaces. Planta 202, 1–8. https://doi.org/10.1007/s004250050096.

Barthwal, S., and Lim, S.H. (2019). Rapid fabrication of a dual-scale micro-nanostructured superhydrophobic aluminum surface with delayed condensation and ice formation properties. Soft Matter. 15, 7945–7955. https://doi.org/10.1039/c9sm01256g.

Bhushan, B., and Chae Jung, Y. (2007). Wetting study of patterned surfaces for superhydrophobicity. Ultramicroscopy 107,

1033–1041. https://doi.org/10.1016/j.ultramic.2007.05.002.

Bhushan, B., and Her, E.K. (2010). Fabrication of superhydrophobic surfaces with high and low adhesion inspired from rose petal. Langmuir 26, 8207–8217. https://doi.org/10.1021/la904585j.

Boreyko, J.B., and Collier, C.P. (2013). Delayed frost growth on jumping-drop superhydrophobic surfaces. ACS Nano 7, 1618–1627. https://doi.org/10.1021/nn3055048.

Cassie, A.B.D., and Baxter, S. (1944). Wettability of porous surfaces. Trans. Faraday Soc. 40. https://doi.org/10.1039/tf9444000546.

Chen, J., Liu, J., He, M., Li, K., Cui, D., Zhang, Q., Zeng, X., Zhang, Y., Wang, J., and Song, Y. (2012). Superhydrophobic surfaces cannot reduce ice adhesion. Appl. Phys. Lett. 101. https://doi.org/10.1063/1.4752436.

Chen, Y., Wang, H., Yao, Q., Fan, B., Wang, C., Xiong, Y., Jin, C., and Sun, Q. (2017). Biomimetic taro leaf-like films decorated on wood surfaces using soft lithography for superparamagnetic and superhydrophobic performance. J. Mater. Sci. 52, 7428–7438. https://doi.org/10.1007/s10853-017-0976-y.

Chen, Y., Jie, Y., Wang, J., Ma, J., Jia, X., Dou, W., and Cao, X. (2018). Triboelectrification on natural rose petal for harvesting environmental mechanical energy. Nano Energy 50, 441–447. https://doi.org/10.1016/j.nanoen.2018.05.021.

Cho, H., Lee, J., Lee, S., and Hwang, W. (2015). Durable superhydrophilic/phobic surfaces based on green patina with corrosion resistance. Phys. Chem. Chem. Phys. 17, 6786–6793. https://doi.org/10.1039/c4cp05590j.

Chu, Z., and Seeger, S. (2014). Superamphiphobic surfaces. Chem. Soc. Rev. 43, 2784–2798. https://doi.org/10.1039/c3cs60415b.

Chu, Z., Jiao, W., Huang, Y., Yan, M., Zheng, Y., Wang, R., and He, X. (2020). Smart superhydrophobic films with self-sensing and anti-icing properties based on silica nanoparticles and graphene. Adv. Mater. Interfaces 7. https://doi.org/10.1002/admi.202000492.

Cui, W., Jiang, Y., Mielonen, K., and Pakkanen, T.A. (2019). The verification of icephobic performance on biomimetic superhydrophobic surfaces and the effect of wettability and surface energy. Appl. Surf. Sci. 466, 503–514. https://doi.org/10.1016/j.apsusc.2018.10.042.

Dalawai, S.P., Saad Aly, M.A., Latthe, S.S., Xing, R., Sutar, R.S., Nagappan, S., Ha, C.-S., Kumar Sadasivuni, K., and Liu, S. (2020). Recent Advances in durability of superhydrophobic self-cleaning technology: a critical review. Prog. Org. Coat. 138. https://doi.org/10.1016/j.porgcoat.2019.105381.

Dong, R., Wang, L., Zhu, J., Liu, L., and Qian, Y. (2019). A novel SiO2–GO/acrylic resin nanocomposite: fabrication, characterization and properties. Appl. Phys. A 125. https://doi.org/10.1007/s00339-019-2847-7.

Duc, N.B., and Binh, N.T. (2020). Investigate on structure for transparent anti-icing surfaces. AIP Adv. 10. https://doi.org/10.1063/5.0019119.

Eberle, P., Tiwari, M.K., Maitra, T., and Poulikakos, D. (2014). Rational nanostructuring of surfaces for extraordinary icephobicity. Nanoscale 6, 4874–4881. https://doi.org/10.1039/c3nr06644d.

Enomoto, K., Kikuchi, M., Narumi, A., and Kawaguchi, S. (2018). Surface modifier-free organic-inorganic hybridization to produce optically transparent and highly refractive bulk materials composed of epoxy resins and ZrO2 nanoparticles. ACS Appl. Mater. Interfaces 10, 13985–13998. https://doi.org/10.1021/acsami.8b00422.

Ensikat, H.J., Ditsche-Kuru, P., Neinhuis, C., and Barthlott, W. (2011). Superhydrophobicity in perfection: the outstanding properties of the lotus leaf. Beilstein J. Nanotechnol. 2, 152–161. https://doi.org/10.3762/bjnano.2.19.

Esmeryan, K.D. (2020). From extremely water-repellent coatings to passive icing protection—principles, limitations and innovative application aspects. Coatings 10. https://doi.org/10.3390/coatings10010066.

Fan, K., Jin, Z., Zhu, X., Wang, Q., and Sun, J. (2019). A facile electrochemical machining process to fabricate superhydrophobic surface on iron materials and its applications in anti-icing. J. Dispersion Sci. Technol. 42, 457–464. https://doi.org/10.1080/01932691.2019.1699429.

Feng, L., Yan, Z., Shi, X., and Sultonzoda, F. (2018). Anti-icing/frosting and self-cleaning performance of superhydrophobic aluminum alloys. Appl. Phys. A 124. https://doi.org/10.1007/s00339-017-1509-x.

Fromel, M., Li, M., and Pester, C.W. (2020). Surface engineering with polymer brush photolithography. Macromol. Rapid Commun. 41, e2000177. https://doi.org/10.1002/marc.202000177.

Gao, X., and Jiang, L. (2004). Biophysics: water-repellent legs of water striders. Nature 432, 36. https://doi.org/10.1038/432036a.

Gauthier, A., Symon, S., Clanet, C., and Quere, D. (2015). Water impacting on superhydrophobic macrotextures. Nat. Commun. 6, 8001. https://doi.org/10.1038/ncomms9001.

Ge, M., Cao, C., Liang, F., Liu, R., Zhang, Y., Zhang, W., Zhu, T., Yi, B., Tang, Y., and Lai, Y. (2020). A "PDMS-in-water" emulsion enables mechanochemically robust superhydrophobic surfaces with self-healing nature. Nanoscale Horizons 5, 65–73. https://doi.org/10.1039/c9nh00519f.

Geim, A.K. (2009). Graphene: status and prospects. Science 324, 1530–1534. https://doi.org/10.1126/science.1158877.

Gohari, B., Russell, K., Hejazi, V., and Rohatgi, P. (2017). Role of water solidification concepts in designing nano-textured anti-icing surfaces. J. Phys. Chem. B 121, 7527–7535. https://doi.org/10.1021/acs.jpcb.7b04081.

Golovin, K., and Tuteja, A. (2017). A predictive framework for the design and fabrication of icephobic polymers. Sci. Adv. 3, e1701617. https://doi.org/10.1126/sciadv.1701617.

Gong, X., Gao, X., and Jiang, L. (2017). Recent progress in bionic condensate microdrop self-propelling surfaces. Adv. Mater. 29. https://doi.org/10.1002/adma.201703002.

Gou, X., and Guo, Z. (2018). Superhydrophobic plant leaves with micro-line structures: an optimal biomimetic objective in bionic engineering. J. Bionic Eng. 15, 851–858. https://doi.org/10.1007/s42235-018-0072-2.

Guo, H., Xing, Y., Yuan, H., Zhang, R., Zhang, Y., and Deng, P. (2019). Improving the anti-icing performance of superhydrophobic surfaces by nucleation inhibitor. Surf. Eng. 36, 621–627. https://doi.org/10.1080/02670844.2019.1677291.

Guo, H., Liu, M., Xie, C., Zhu, Y., Sui, X., Wen, C., Li, Q., Zhao, W., Yang, J., and Zhang, L. (2020). A sunlight-responsive and robust anti-icing/deicing coating based on the amphiphilic materials. Chem. Eng. J. 402. https://doi.org/10.1016/j.cej.2020.126161.

He, M., Wang, J., Li, H., and Song, Y. (2011). Super-hydrophobic surfaces to condensed micro-droplets at temperatures below the freezing point retard ice/frost formation. Soft Matter 7. https://doi.org/10.1039/c0sm01504k.

He, M., Zhang, Q., Zeng, X., Cui, D., Chen, J., Li, H., Wang, J., and Song, Y. (2013). Hierarchical porous surface for efficiently controlling microdroplets' self-removal. Adv. Mater. 25, 2291–2295. https://doi.org/10.1002/adma.201204660.

He, T., Liu, X., Wang, Y., Wu, D., Liu, Y., and Liu, X. (2020). Fabrication of durable hierarchical superhydrophobic fabrics with Sichuan pepper-like structures via graft precipitation polymerization. Appl. Surf. Sci. 529. https://doi.org/10.1016/j.apsusc.2020.147017.

Hu, J., and Jiang, G. (2020). Superhydrophobic coatings on iodine doped substrate with photothermal deicing and passive anti-icing properties. Surf. Coat. Technol. 402. https://doi.org/10.1016/j.surfcoat.2020.126342.

Ibrahim, Y., Kempers, R., and Amirfazli, A. (2019). 3D printed electro-thermal anti- or de-icing system for composite panels. Cold Reg. Sci. Technol. 166. https://doi.org/10.1016/j.coldregions.2019.102844.

Jeevahan, J., Chandrasekaran, M., Britto Joseph, G., Durairaj, R.B., and Mageshwaran, G. (2018). Superhydrophobic surfaces: a review on fundamentals, applications, and challenges. J. Coat. Technol. Res. 15, 231–250. https://doi.org/10.1007/s11998-017-0011-x.

Jia, Z., Shen, Y., Tao, J., Zhang, Y., Chen, H., Lu, Y., and Wu, Z. (2020). Understanding the solid–ice interface mechanism on the hydrophobic nano-pillar structure epoxy surface for reducing ice adhesion. Coatings 10. https://doi.org/10.3390/coatings10111043.

Jiang, L., Zhao, Y., and Zhai, J. (2004). A lotus-leaf-like superhydrophobic surface: a porous microsphere/nanofiber composite film prepared by electrohydrodynamics. Angew. Chem. Int. Ed. 43, 4338–4341. https://doi.org/10.1002/anie.200460333.

Jiang, G., Chen, L., Zhang, S., and Huang, H. (2018). Superhydrophobic SiC/CNTs coatings with photothermal deicing and passive anti-icing properties. ACS Appl. Mater. Interfaces 10,

36505–36511. https://doi.org/10.1021/acsami.8b11201.

Jin, S., Liu, J., Lv, J., Wu, S., and Wang, S.J. (2018). Interfacial materials for anti-icing: beyond superhydrophobic surfaces. Chem. Asian J. 13, 1406–1414. https://doi.org/10.1002/asia.201800241.

Jing, X., and Guo, Z. (2018). Biomimetic super durable and stable surfaces with superhydrophobicity. J. Mater. Chem. A 6, 16731–16768. https://doi.org/10.1039/c8ta04994g.

Khadak, A., Subeshan, B., and Asmatulu, R. (2020). Studies on de-icing and anti-icing of carbon fiber-reinforced composites for aircraft surfaces using commercial multifunctional permanent superhydrophobic coatings. J. Mater. Sci. 56, 3078–3094. https://doi.org/10.1007/s10853-020-05459-9.

Khanmohammadi Chenab, K. (2020). Anti-icing properties of vertically aligned TiO2 nanopillars. Langmuir 36, 6041–6050. https://doi.org/10.1021/acs.langmuir.0c00093.

Khanzadeh Borjak, S., Rafee, R., and Valipour, M.S. (2020). Experimental investigation of water droplet impact on the electrospun superhydrophobic cylindrical glass: contact time, maximum spreading factor, and splash threshold. Langmuir 36, 13498–13508. https://doi.org/10.1021/acs.langmuir.0c02228.

Kreder, M.J., Alvarenga, J., Kim, P., and Aizenberg, J. (2016). Design of anti-icing surfaces: smooth, textured or slippery? Nat. Rev. Mater. 1. https://doi.org/10.1038/natrevmats.2015.3.

Lafuma, A., and Quere, D. (2003). Superhydrophobic states. Nat. Mater. 2, 457–460. https://doi.org/10.1038/nmat924.

Lagubeau, G., Fontelos, M.A., Josserand, C., Maurel, A., Pagneux, V., and Petitjeans, P. (2012). Spreading dynamics of drop impacts. J. Fluid Mech. 713, 50–60. https://doi.org/10.1017/jfm.2012.431.

Latthe, S.S., Sutar, R.S., Bhosale, A.K., Nagappan, S., Ha, C.-S., Sadasivuni, K.K., Liu, S., and Xing, R. (2019). Recent developments in air-trapped superhydrophobic and liquid-infused slippery surfaces for anti-icing application. Prog. Org. Coat. 137. https://doi.org/10.1016/j.porgcoat.2019.105373.

Lee, S.H., Seong, M., Kwak, M.K., Ko, H., Kang, M., Park, H.W., Kang, S.M., and Jeong, H.E. (2018a). Tunable multimodal drop bouncing dynamics and anti-icing performance of a magnetically responsive hair array. ACS Nano 12, 10693–10702. https://doi.org/10.1021/acsnano.8b05109.

Lee, Y., You, E.A., and Ha, Y.G. (2018b). Rationally designed, multifunctional self-assembled nanoparticles for covalently networked, flexible and self-healable superhydrophobic composite films. ACS Appl. Mater. Interfaces 10, 9823–9831. https://doi.org/10.1021/acsami.7b19045.

Lei, S., Wang, F., Fang, X., Ou, J., and Li, W. (2019). Icing behavior of water droplets impinging on cold superhydrophobic surface. Surf. Coat. Technol. 363, 362–368. https://doi.org/10.1016/j.surfcoat.2019.02.035.

Li, Q., and Guo, Z. (2018). Fundamentals of icing and common strategies for designing biomimetic anti-icing surfaces. J. Mater. Chem. A 6, 13549–13581. https://doi.org/10.1039/c8ta03259a.

Li, L., Li, B., Dong, J., and Zhang, J. (2016). Roles of silanes and silicones in forming superhydrophobic and superoleophobic materials. J. Mater. Chem. A 4, 13677–13725. https://doi.org/10.1039/c6ta05441b.

Li, Y., Li, B., Zhao, X., Tian, N., and Zhang, J. (2018a). Totally waterborne, nonfluorinated, mechanically robust, and self-healing superhydrophobic coatings for actual anti-icing. ACS Appl. Mater. Interfaces 10, 39391–39399. https://doi.org/10.1021/acsami.8b15061.

Li, Y., Zhan, X., Gao, C., Wang, H., and Yang, Y. (2019a). Comparative study of infrared laser surface laser surface treatment and ultraviolet laser surface treatment of CFRP laminates. Int. J. Adv. Manuf. Technol. 102, 4059–4071. https://doi.org/10.1007/s00170-019-03368-z.

Li, J., Wang, W., Mei, X., Pan, A., Sun, X., Liu, B., and Cui, J. (2019b). Artificial compound eyes prepared by a combination of air-assisted deformation, modified laser swelling, and controlled crystal growth. ACS Nano 13, 114–124. https://doi.org/10.1021/acsnano.8b04047.

Li, Z., Cao, M., Li, P., Zhao, Y., Bai, H., Wu, Y., and Jiang, L. (2019c). Surface-embedding of functional micro-/nanoparticles for achieving versatile superhydrophobic interfaces. Matter 1, 661–673. https://doi.org/10.1016/j.matt.2019.03.009.

Li, J., Wang, W., Mei, X., and Pan, A. (2020). Effects of surface wettability on the dewetting performance of hydrophobic surfaces. ACS Omega 5, 28776–28783. https://doi.org/10.1021/acsomega.0c04106.

Li, W., Zhan, Y., and Yu, S. (2021). Applications of superhydrophobic coatings in anti-icing: theory, mechanisms, impact factors, challenges and perspectives. Prog. Org. Coat. 152. https://doi.org/10.1016/j.porgcoat.2020.106117.

Lin, Y., Chen, H., Wang, G., and Liu, A. (2018). Recent progress in preparation and anti-icing applications of superhydrophobic coatings. Coatings 8. https://doi.org/10.3390/coatings8060208.

Liu, H., Huang, J., Chen, Z., Chen, G., Zhang, K.-Q., Al-Deyab, S.S., and Lai, Y. (2017). Robust translucent superhydrophobic PDMS/PMMA film by facile one-step spray for self-cleaning and efficient emulsion separation. Chem. Eng. J. 330, 26–35. https://doi.org/10.1016/j.cej.2017.07.114.

Liu, C., Zhu, L., Li, J., and Liang, Y. (2019a). Fabrication of superhydrophobic bionic surface integrating with VOF simulation studies of liquid drop impacting. Microsc. Res. Tech. 82, 615–623. https://doi.org/10.1002/jemt.23208.

Liu, W., Chen, H., Shen, Y., and Wu, Z. (2019b). Facilely fabricating superhydrophobic resin-based coatings with lower water freezing temperature and ice adhesion for anti-icing application. J. Bionic Eng. 16, 794–805. https://doi.org/10.1007/s42235-019-0097-1.

Liu, W., Wang, C., Zhang, L., Pan, H., Liu, W., Chen, J., Yang, D., Xiang, Y., Wang, K., Jiang, J.,

and Yao, X. (2019c). Exfoliation of amorphous phthalocyanine conjugated polymers into ultrathin nanosheets for highly efficient oxygen reduction. J. Mater. Chem. A 7, 3112–3119. https://doi.org/10.1039/c8ta11044a.

Liu, X., Wang, K., Zhang, W., Zhang, J., and Li, J. (2019d). Robust, self-cleaning, anti-fouling, superamphiphobic soy protein isolate composite films using spray-coating technique with fluorinated HNTs/SiO2. Compos. B Eng. 174. https://doi.org/10.1016/j.compositesb.2019.107002.

Liu, H.-d., Zhang, H., Pang, J., Ning, Y.-J., Jia, F., Yuan, W.-F., Gu, B., and Zhang, Q.-P. (2019e). Superhydrophobic property of epoxy resin coating modified with octadecylamine and SiO2 nanoparticles. Mater. Lett. 247, 204–207. https://doi.org/10.1016/j.matlet.2019.03.128.

Liu, C., Liu, Q., Jin, R., Lin, Z., Qiu, H., and Xu, Y. (2020a). Mechanism analysis and durability evaluation of anti-icing property of superhydrophobic surface. Int. J. Heat Mass Transfer 156. https://doi.org/10.1016/j.ijheatmasstransfer.2020.119768.

Liu, R., Chi, Z., Cao, L., Weng, Z., Wang, L., Li, L., Saeed, S., Lian, Z., and Wang, Z. (2020b). Fabrication of biomimetic superhydrophobic and anti-icing Ti6Al4V alloy surfaces by direct laser interference lithography and hydrothermal treatment. Appl. Surf. Sci. 534. https://doi.org/10.1016/j.apsusc.2020.147576.

Lu, H., Zheng, Y., Yin, W., Tao, D., Pesika, N., Meng, Y., and Tian, Y. (2018). Propulsion principles of water striders in sculling forward through shadow method. J. Bionic Eng. 15, 516–525. https://doi.org/10.1007/s42235-018-0042-8.

Luo, S., Wang, J., and Li, Z. (2020). Homogeneous ice nucleation under shear. J. Phys. Chem. B 124, 3701–3708. https://doi.org/10.1021/acs.jpcb.9b11209.

Lv, J., Song, Y., Jiang, L., and Wang, J. (2014). Bio-inspired strategies for anti-icing. ACS Nano 8, 3152–3169. https://doi.org/10.1021/nn406522n.

Lv, J., Wang, B., Ma, Q., Wang, W., Zeng, L., Li, M., Li, A., Zhao, X., Li, J., Xiang, Q., et al. (2018). Preparation of superhydrophobic melamine sponges decorated with polysiloxane nanotubes by plasma enhanced chemical vapor deposition (PECVD) method for oil/water separation. Mater. Res. Express 5. https://doi.org/10.1088/2053-1591/aad0e1.

Lv, L., Liu, H., Zhang, W., Chen, J., and Liu, Z. (2020). Facile UV-curable fabrication of robust, anti-icing superhydrophobic coatings based on polyurethane. Mater. Lett. 258. https://doi.org/10.1016/j.matlet.2019.126653.

Miljkovic, N., Enright, R., Nam, Y., Lopez, K., Dou, N., Sack, J., and Wang, E.N. (2013). Jumping-droplet-enhanced condensation on scalable superhydrophobic nanostructured surfaces. Nano Lett. 13, 179–187. https://doi.org/10.1021/nl303835d.

Miljkovic, N., Preston, D.J., Enright, R., and Wang, E.N. (2014). Jumping-droplet electrostatic energy harvesting. Appl. Phys. Lett. 105. https://doi.org/10.1063/1.4886798.

Mouterde, T., Lehoucq, G., Xavier, S., Checco, A., Black, C.T., Rahman, A., Midavaine, T., Clanet, C., and Quere, D. (2017). Antifogging abilities of model nanotextures. Nat. Mater. 16, 658–663. https://doi.org/10.1038/nmat4868.

Mundo, C., Sommerfeld, M., and Tropea, C. (1995). Droplet-wall collisions: experimental studies of the deformation and breakup process. Int. J. Multiphase Flow 21, 151–173. https://doi.org/10.1016/0301-9322(94)00069-v.

Nguyen, T.-B., Park, S., and Lim, H. (2018). Effects of morphology parameters on anti-icing performance in superhydrophobic surfaces. Appl. Surf. Sci. 435, 585–591. https://doi.org/10.1016/j.apsusc.2017.11.137.

Nguyen, B.D., Cao, B.X., Do, T.C., Trin, H.B., and Nguyen, T.B. (2019). Interfacial parameters in correlation with anti-icing performance. J. Adhes. 1–13. https://doi.org/10.1080/00218464.2019.1709172.

Niu, H., Yang, Y.I., and Parrinello, M. (2019). Temperature dependence of homogeneous nucleation in ice. Phys. Rev. Lett. 122, 245501. https://doi.org/10.1103/PhysRevLett.122.245501.

Pan, L., Wang, F., Pang, X., Zhang, L., and Hao, J. (2019). Superhydrophobicity and anti-icing of CF/PEEK composite surface with hierarchy structure. J. Mater. Sci. 54, 14728–14741. https://doi.org/10.1007/s10853-019-03956-0.

Pan, L., Liu, Z., kızıltaş, O., Zhong, L., Pang, X., Wang, F., Zhu, Y., Ma, W., and Lv, Y. (2020). Carbon fiber/poly ether ether ketone composites modified with graphene for electro-thermal deicing applications. Compos. Sci. Technol. 192. https://doi.org/10.1016/j.compscitech.2020.108117.

Peng, C., Hu, X., You, Z., Xu, F., Jiang, G., Ouyang, H., Guo, C., Ma, H., Lu, L., and Dai, J. (2020). Investigation of anti-icing, anti-skid, and water impermeability performances of an acrylic superhydrophobic coating on asphalt pavement. Constr. Build. Mater. 264. https://doi.org/10.1016/j.conbuildmat.2020.120702.

Qi, Y., Chen, S., and Zhang, J. (2019). Fluorine modification on titanium dioxide particles: improving the anti-icing performance through a very hydrophobic surface. Appl. Surf. Sci. 476, 161–173. https://doi.org/10.1016/j.apsusc.2019.01.073.

Qi, C., Chen, H., Sun, Y., Fu, Q., shen, L., Li, X., and Liu, Y. (2020a). Facile synthesis and anti-icing performance of superhydrophobic flower-like OTS-SiO2 with tunable size. Adv. Powder Technol. 31, 4533–4540. https://doi.org/10.1016/j.apt.2020.09.029.

Qi, Y., Yang, Z., Chen, T., Xi, Y., and Zhang, J. (2020b). Fabrication of superhydrophobic surface with desirable anti-icing performance based on micro/nano-structures and organosilane groups. Appl. Surf. Sci. 501. https://doi.org/10.1016/j.apsusc.2019.144165.

Qi, C., Chen, H., Shen, L., Li, X., Fu, Q., Zhang, Y., Sun, Y., and Liu, Y. (2020c). Superhydrophobic surface based on assembly of nanoparticles for application in anti-icing under ultralow temperature. ACS Appl. Nano Mater. 3, 2047–2057. https://doi.org/10.1021/acsanm.0c00220.

Qing, Y., Long, C., An, K., Hu, C., and Liu, C. (2019). Sandpaper as template for a robust superhydrophobic surface with self-cleaning and anti-snow/icing performances. J. Colloid Interface Sci. 548, 224–232. https://doi.org/10.1016/j.jcis.2019.04.040.

Qiu, R., Li, Z., and Wu, Z. (2019). Enhanced anti-icing and anti-corrosion properties of wear-resistant superhydrophobic surfaces based on Al alloys. Mater. Res. Express 6. https://doi.org/10.1088/2053-1591/aafdf1.

Ramakrishna, D.M. (2005). Environmental impact of chemical deicers—A review 15. https://doi.org/10.1007/s11270-005-8265-9.

Richard, D., Clanet, C., and Quere, D. (2002). Contact time of a bouncing drop. Nature 417, 811. https://doi.org/10.1038/417811a.

Roh, S.C., Choi, E.Y., Choi, Y.S., and Kim, C.K. (2014). Characterization of the surface energies of functionalized multi-walled carbon nanotubes and their interfacial adhesion energies with various polymers. Polymer 55, 1527–1536. https://doi.org/10.1016/j.polymer.2014.02.015.

Ryu, J., Kim, K., Park, J., Hwang, B.G., Ko, Y., Kim, H., Han, J., Seo, E., Park, Y., and Lee, S.J. (2017). Nearly perfect durable superhydrophobic surfaces fabricated by a simple one-step plasma treatment. Sci. Rep. 7, 1981. https://doi.org/10.1038/s41598-017-02108-1.

Saji, V.S. (2020). Superhydrophobic surfaces and coatings by electrochemical anodic oxidation and plasma electrolytic oxidation. Adv. Colloid Interf. Sci 283, 102245. https://doi.org/10.1016/j.cis.2020.102245.

Saji, V.S. (2021). Carbon nanostructure-based superhydrophobic surfaces and coatings. Nanotechnol. Rev. 10, 518–571. https://doi.org/10.1515/ntrev-2021-0039.

Sarshar, M.A., Song, D., Swarctz, C., Lee, J., and Choi, C.H. (2018). Anti-icing or deicing: icephobicities of superhydrophobic surfaces with hierarchical structures. Langmuir 34, 13821–13827. https://doi.org/10.1021/acs.langmuir.8b02231.

Schutzius, T.M., Jung, S., Maitra, T., Eberle, P., Antonini, C., Stamatopoulos, C., and Poulikakos, D. (2015). Physics of icing and rational design of surfaces with extraordinary icephobicity. Langmuir 31, 4807–4821. https://doi.org/10.1021/la502586a.

Sear, R.P. (2007). Nucleation: theory and applications to protein solutions and colloidal suspensions. J. Phys. Condensed Matter 19. https://doi.org/10.1088/0953-8984/19/3/033101.

Sebastian, D., Yao, C.-W., and Lian, I. (2018). Mechanical durability of engineered superhydrophobic surfaces for anti-corrosion. Coatings 8. https://doi.org/10.3390/coatings8050162.

Shen, Y., Tao, J., Tao, H., Chen, S., Pan, L., and Wang, T. (2015a). Approaching the theoretical contact time of a bouncing droplet on the rational macrostructured superhydrophobic surfaces. Appl. Phys. Lett. 107. https://doi.org/10.1063/1.4931095.

Shen, Y., Tao, J., Tao, H., Chen, S., Pan, L., and Wang, T. (2015b). Anti-icing potential of superhydrophobic Ti6Al4V surfaces: ice nucleation and growth. Langmuir 31, 10799–10806. https://doi.org/10.1021/acs.langmuir.5b02946.

Shen, Y., Xie, Y., Tao, J., Chen, H., Zhu, C., Jin, M., and Lu, Y. (2018). Rationally designed nanostructure features on superhydrophobic surfaces for enhancing self-propelling dynamics of condensed droplets. ACS Sustainable Chem. Eng. 7, 2702–2708. https://doi.org/10.1021/acssuschemeng.8b05780.

Shen, Y., Wu, X., Tao, J., Zhu, C., Lai, Y., and Chen, Z. (2019a). Icephobic materials: fundamentals, performance evaluation, and applications. Prog. Mater. Sci. 103, 509–557. https://doi.org/10.1016/j.pmatsci.2019.03.004.

Shen, Y., Wu, Y., Tao, J., Zhu, C., Chen, H., Wu, Z., and Xie, Y. (2019b). Spraying fabrication of durable and transparent coatings for anti-icing application: dynamic water repellency, icing delay, and ice adhesion. ACS Appl. Mater. Interfaces 11, 3590–3598. https://doi.org/10.1021/acsami.8b19225.

Shen, Y., Xie, X., Xie, Y., Tao, J., Jiang, J., Chen, H., Lu, Y., and Xu, Y. (2019c). Statistically understanding the roles of nanostructure features in interfacial ice nucleation for enhancing icing delay performance. Phys. Chem. Chem. Phys. 21, 19785–19794. https://doi.org/10.1039/c9cp04103f.

Si, Y., Dong, Z., and Jiang, L. (2018). Bioinspired designs of superhydrophobic and superhydrophilic materials. ACS Cent. Sci. 4, 1102–1112. https://doi.org/10.1021/acscentsci.8b00504.

Smith, A.F.W., Mahelona, K., and Hendy, S.C. (2018). Rolling and slipping of droplets on superhydrophobic surfaces. Phys. Rev. E 98. https://doi.org/10.1103/PhysRevE.98.033113.

Subeshan, B., Usta, A., and Asmatulu, R. (2020). Deicing and self-cleaning of plasma-treated superhydrophobic coatings on the surface of aluminum alloy sheets. Surf. Inter. 18. https://doi.org/10.1016/j.surfin.2020.100429.

Sun, Y., and Guo, Z. (2019). Recent advances of bioinspired functional materials with specific wettability: from nature and beyond nature. Nanoscale Horizons 4, 52–76. https://doi.org/10.1039/c8nh00223a.

Sun, R., Zhao, J., Li, Z., Qin, N., Mo, J., Pan, Y., and Luo, D. (2020a). Robust superhydrophobic aluminum alloy surfaces with anti-icing ability, thermostability, and mechanical durability. Prog. Org. Coat. 147. https://doi.org/10.1016/j.porgcoat.2020.105745.

Sun, Y., Sui, X., Wang, Y., Liang, W., and Wang, F. (2020b). Passive anti-icing and active electrothermal deicing system based on an ultraflexible carbon nanowire (CNW)/PDMS biomimetic nanocomposite with a superhydrophobic microcolumn surface. Langmuir 36, 14483–14494. https://doi.org/10.1021/acs.langmuir.0c01745.

Taherian, F., Marcon, V., van der Vegt, N.F., and Leroy, F. (2013). What is contact angle of

water on graphene? Langmuir *29*, 1457–1465. https://doi.org/10.1021/la304645w.

Talalay, P., Liu, N., Yang, Y., Xu, H., Sysoev, M., and Fan, X. (2019). Ice drills recovery using chemical deicers. Polar Sci. *19*, 49–56. https://doi.org/10.1016/j.polar.2018.08.005.

Tang, Y., Zhang, Q., Zhan, X., and Chen, F. (2015). Superhydrophobic and anti-icing properties at overcooled temperature of a fluorinated hybrid surface prepared via a sol-gel process. Soft Matter *11*, 4540–4550. https://doi.org/10.1039/c5sm00674k.

Tang, L., Wang, N., Han, Z., Sun, H., and Xiong, D. (2020). Robust superhydrophobic surface with wrinkle-like structures on AZ31 alloy that repels viscous oil and investigations of the anti-icing property. Colloids Surf. A Physicochem. Eng. Asp. *594*. https://doi.org/10.1016/j.colsurfa.2020.124655.

Tian, Y., and Wang, L. (2018). Bioinspired microfibers for water collection. J. Mater. Chem. A *6*, 18766–18781. https://doi.org/10.1039/c8ta08104b.

Tong, W., Xiong, D., Wang, N., Yan, C., and Tian, T. (2018). Green and timesaving fabrication of a superhydrophobic surface and its application to anti-icing, self-cleaning and oil-water separation. Surf. Coat. Technol. *352*, 609–618. https://doi.org/10.1016/j.surfcoat.2018.08.035.

Tong, W., Xiong, D., Wang, N., Wu, Z., and Zhou, H. (2019). Mechanically robust superhydrophobic coating for aeronautical composite against ice accretion and ice adhesion. Compos. Part B Eng. *176*. https://doi.org/10.1016/j.compositesb.2019.107267.

Vandadi, A., Zhao, L., and Cheng, J. (2019). Resistant energy analysis of self-pulling process during dropwise condensation on superhydrophobic surfaces. Nanoscale Adv. *1*, 1136–1147. https://doi.org/10.1039/c8na00237a.

Varanasi, K.K., Hsu, M., Bhate, N., Yang, W., and Deng, T. (2009). Spatial control in the heterogeneous nucleation of water. Appl. Phys. Lett. *95*. https://doi.org/10.1063/1.3200951.

Villeneuve, E., Brassard, J.-D., and Volat, C. (2019). Effect of various surface coatings on de-icing/anti-icing fluids aerodynamic and endurance time performances. Aerospace *6*. https://doi.org/10.3390/aerospace6100114.

Wang, F., and Guo, Z. (2019). Facile synthesis of superhydrophobic three-metal-component layered double hydroxide films on aluminum foils for highly improved corrosion inhibition. N. J. Chem. *43*, 2289–2298. https://doi.org/10.1039/c8nj05732j.

Wang, J., Zheng, Y., Nie, F.Q., Zhai, J., and Jiang, L. (2009a). Air bubble bursting effect of lotus leaf. Langmuir *25*, 14129–14134. https://doi.org/10.1021/la9010828.

Wang, S., Zhang, Y., Abidi, N., and Cabrales, L. (2009b). Wettability and surface free energy of graphene films. Langmuir *25*, 11078–11081. https://doi.org/10.1021/la901402f.

Wang, Y., Xue, J., Wang, Q., Chen, Q., and Ding, J. (2013). Verification of icephobic/anti-icing properties of a superhydrophobic surface. ACS

Appl. Mater. Interfaces *5*, 3370–3381. https://doi.org/10.1021/am400429q.

Wang, S., Yang, Z., Gong, G., Wang, J., Wu, J., Yang, S., and Jiang, L. (2016). Icephobicity of PenguinsSpheniscus humboldtiand an artificial replica of penguin feather with air-infused hierarchical rough structures. J. Phys. Chem. C *120*, 15923–15929. https://doi.org/10.1021/acs.jpcc.5b12298.

Wang, S., Yu, X., Liang, C., and Zhang, Y. (2018). Enhanced condensation heat transfer in air-conditioner heat exchanger using superhydrophobic foils. Appl. Therm. Eng. *137*, 758–766. https://doi.org/10.1016/j.applthermaleng.2018.04.020.

Wang, J., Memon, H., Liu, J., Yang, G., Xu, F., Hussain, M., Scotchford, C., and Hou, X. (2019a). Effect of surface adsorption on icing behaviour of metallic coating. Surf. Coat. Technol. *380*. https://doi.org/10.1016/j.surfcoat.2019.125068.

Wang, H., He, M., Liu, H., and Guan, Y. (2019b). One-step fabrication of robust superhydrophobic steel surfaces with mechanical durability, thermal stability, and anti-icing function. ACS Appl. Mater. Interfaces *11*, 25586–25594. https://doi.org/10.1021/acsami.9b06865.

Wang, F., Pi, J., Song, F., Feng, R., Xu, C., Wang, X.-L., and Wang, Y.-Z. (2020a). A superhydrophobic coating to create multi-functional materials with mechanical/chemical/physical robustness. Chem. Eng. J. *381*. https://doi.org/10.1016/j.cej.2019.122539.

Wang, P., Yao, T., Li, Z., Wei, W., Xie, Q., Duan, W., and Han, H. (2020b). A superhydrophobic/electrothermal synergistically anti-icing strategy based on graphene composite. Compos. Sci. Technol. *198*. https://doi.org/10.1016/j.compscitech.2020.108307.

Wang, D., Sun, Q., Hokkanen, M.J., Zhang, C., Lin, F.Y., Liu, Q., Zhu, S.P., Zhou, T., Chang, Q., He, B., et al. (2020c). Design of robust superhydrophobic surfaces. Nature *582*, 55–59. https://doi.org/10.1038/s41586-020-2331-8.

Wang, G.F., Zhou, W., Zhou, J., Wang, M.M., Zhang, Y.B., and Qiang, H. (2021a). Superhydrophobic silicone rubber surface prepared by direct replication. Surf. Eng. *37*, 278–287. https://doi.org/10.1080/02670844.2020.1776669.

Wang, J., Wang, H., Wang, Y., Gao, P., Wang, F., Men, X., Zhang, Z., and Lu, Y. (2021b). Design robust, degradable and recyclable superhydrophobic materials. Chem. Eng. J. *420*. https://doi.org/10.1016/j.cej.2021.129806.

Wei, K., Yang, Y., Zuo, H., and Zhong, D. (2019). A review on ice detection technology and ice elimination technology for wind turbine. Wind Energy *23*, 433–457. https://doi.org/10.1002/we.2427.

Wen, R., Xu, S., Zhao, D., Lee, Y.C., Ma, X., and Yang, R. (2017). Hierarchical superhydrophobic surfaces with micropatterned nanowire arrays for high-efficiency jumping droplet condensation. ACS Appl. Mater. Interfaces *9*, 44911–44921. https://doi.org/10.1021/acsami.7b14960.

Wenzel, R.N. (2002). Resistance of solid surfaces to wetting by water. Ind. Eng. Chem. *28*, 988–994. https://doi.org/10.1021/ie50320a024.

Wu, X., and Chen, Z. (2018). A mechanically robust transparent coating for anti-icing and self-cleaning applications. J. Mater. Chem. A *6*, 16043–16052. https://doi.org/10.1039/c8ta05692g.

Wu, Y., Shen, Y., Tao, J., He, Z., Xie, Y., Chen, H., Jin, M., and Hou, W. (2018a). Facile spraying fabrication of highly flexible and mechanically robust superhydrophobic F-SiO2@PDMS coatings for self-cleaning and drag-reduction applications. New J. Chem. *42*, 18208–18216. https://doi.org/10.1039/c8nj04275f.

Wu, X., Zheng, S., Bellido-Aguilar, D.A., Silberschmidt, V.V., and Chen, Z. (2018b). Transparent icephobic coatings using bio-based epoxy resin. Mater. Des. *140*, 516–523. https://doi.org/10.1016/j.matdes.2017.12.017.

Wu, X., Silberschmidt, V.V., Hu, Z.-T., and Chen, Z. (2019a). When superhydrophobic coatings are icephobic: role of surface topology. Surf. Coat. Technol. *358*, 207–214. https://doi.org/10.1016/j.surfcoat.2018.11.039.

Wu, S., He, Z., Zang, J., Jin, S., Wang, Z., Wang, J., Yao, Y., and Wang, J. (2019b). Heterogeneous ice nucleation correlates with bulk-like interfacial water. Sci. Adv. *5*, eaat9825. https://doi.org/10.1126/sciadv.aat9825.

Wu, Y.-l., She, W., Shi, D., Jiang, T., Hao, T.-h., Liu, J., Zhang, Q.-c., You, J., and Li, R.Y. (2020). An extremely chemical and mechanically durable siloxane bearing copolymer coating with self-crosslinkable and anti-icing properties. Compos. B Eng. *195*. https://doi.org/10.1016/j.compositesb.2020.108031.

Xiang, G.-X., Li, S.-Y., Song, H., and Nan, Y.-G. (2020). Fabrication of modifier-free superhydrophobic surfaces with anti-icing and self-cleaning properties on Ti substrate by anodization method. Microelectron. Eng. *233*. https://doi.org/10.1016/j.mee.2020.111430.

Xie, Y., Chen, H., Shen, Y., Tao, J., Jin, M., Wu, Y., and Hou, W. (2019). Rational fabrication of superhydrophobic nanocone surface for dynamic water repellency and anti-icing potential. J. Bionic Eng. *16*, 27–37. https://doi.org/10.1007/s42235-019-0003-x.

Xing, D., Wang, R., Wu, F., and Gao, X. (2020). Confined growth and controlled coalescence/self-removal of condensate microdrops on a spatially heterogeneously patterned superhydrophilic-superhydrophobic surface. ACS Appl. Mater. Interfaces *12*, 29946–29952. https://doi.org/10.1021/acsami.0c04922.

Yan, X., Zhang, L., Sett, S., Feng, L., Zhao, C., Huang, Z., Vahabi, H., Kota, A.K., Chen, F., and Miljkovic, N. (2019a). Droplet jumping: effects of droplet size, surface structure, pinning, and liquid properties. ACS Nano *13*, 1309–1323. https://doi.org/10.1021/acsnano.8b06677.

Yan, X., Huang, Z., Sett, S., Oh, J., Cha, H., Li, L., Feng, L., Wu, Y., Zhao, C., Orejon, D., et al. (2019b). Atmosphere-mediated superhydrophobicity of rationally designed micro/nanostructured surfaces. ACS Nano *13*,

4160–4173. https://doi.org/10.1021/acsnano.8b09106.

Yan, X., Qin, Y., Chen, F., Zhao, G., Sett, S., Hoque, M.J., Rabbi, K.F., Zhang, X., Wang, Z., Li, L., et al. (2020). Laplace pressure driven single-droplet jumping on structured surfaces. ACS Nano 14, 12796–12809. https://doi.org/10.1021/acsnano.0c03487.

Yi, M., Liu, L., Wu, L., and Li, X. (2019). Research on sliding angles of water droplets on the hierarchical structured superhydrophobic surfaces. Appl. Phys. A 126. https://doi.org/10.1007/s00339-019-3137-0.

Yin, Z., Xue, M., Luo, Y., Hong, Z., Xie, C., Ren, Z., and Wang, H. (2020). Excellent static and dynamic anti-icing properties of hierarchical structured ZnO superhydrophobic surface on Cu substrates. Chem. Phys. Lett. 755. https://doi.org/10.1016/j.cplett.2020.137806.

Yu, S., Guo, Z., and Liu, W. (2015). Biomimetic transparent and superhydrophobic coatings: from nature and beyond nature. Chem. Commun. (Camb) 51, 1775–1794. https://doi.org/10.1039/c4cc06868h.

Zhan, X., Yan, Y., Zhang, Q., and Chen, F. (2014). A novel superhydrophobic hybrid nanocomposite material prepared by surface-initiated AGET ATRP and its anti-icing properties. J. Mater. Chem. A. 2, 9390–9399. https://doi.org/10.1039/c4ta00634h.

Zhang, Z., and Liu, X.Y. (2018). Control of ice nucleation: freezing and antifreeze strategies.

Chem. Soc. Rev. 47, 7116–7139. https://doi.org/10.1039/c8cs00626a.

Zhang, S., Huang, J., Cheng, Y., Yang, H., Chen, Z., and Lai, Y. (2017). Bioinspired surfaces with superwettability for anti-icing and ice-phobic application: concept, mechanism, and design. Small 13. https://doi.org/10.1002/smll.201701867.

Zhang, X., Ding, B., Bian, Y., Jiang, D., and Parkin, I.P. (2018). Synthesis of superhydrophobic surfaces with Wenzel and Cassie-Baxter state: experimental evidence and theoretical insight. Nanotechnology 29, 485601. https://doi.org/10.1088/1361-6528/aae187.

Zhang, Y., Zhang, L., Xiao, Z., Wang, S., and Yu, X. (2019a). Fabrication of robust and repairable superhydrophobic coatings by an immersion method. Chem. Eng. J. 369, 1–7. https://doi.org/10.1016/j.cej.2019.03.021.

Zhang, H.Y., Yang, Y.L., Pan, J.F., Long, H., Huang, L.S., and Zhang, X.K. (2019b). Compare study between icephobicity and superhydrophobicity. Physica B Condens. Matter 556, 118–130. https://doi.org/10.1016/j.physb.2018.12.014.

Zhang, C., Liang, F., Zhang, W., Liu, H., Ge, M., Zhang, Y., Dai, J., Wang, H., Xing, G., Lai, Y., and Tang, Y. (2020). Constructing mechanochemical durable and self-healing superhydrophobic surfaces. ACS Omega 5, 986–994. https://doi.org/10.1021/acsomega.9b03912.

Zhao, Z., Chen, H., Liu, X., Liu, H., and Zhang, D. (2018). Development of high-efficient synthetic

electric heating coating for anti-icing/de-icing. Surf. Coat. Technol. 349, 340–346. https://doi.org/10.1016/j.surfcoat.2018.06.011.

Zheng, Y., Gao, X., and Jiang, L. (2007). Directional adhesion of superhydrophobic butterfly wings. Soft Matter 3, 178–182. https://doi.org/10.1039/b612667g.

Zheng, H., Chang, S., Ma, G., and Wang, S. (2020). Anti-icing performance of superhydrophobic surface fabricated by femtosecond laser composited dual-layers coating. Energy Build. 223. https://doi.org/10.1016/j.enbuild.2020.110175.

Zhou, H., Chen, R., Liu, Q., Liu, J., Yu, J., Wang, C., Zhang, M., Liu, P., and Wang, J. (2019a). Fabrication of ZnO/epoxy resin superhydrophobic coating on AZ31 magnesium alloy. Chem. Eng. J. 368, 261–272. https://doi.org/10.1016/j.cej.2019.02.032.

Zhou, X., Yu, S., Jiao, S., Lv, Z., Liu, E., Zhao, Y., and Cao, N. (2019b). Fabrication of superhydrophobic TiO2 quadrangular nanorod film with self-cleaning, anti-icing properties. Ceramics Int. 45, 11508–11516. https://doi.org/10.1016/j.ceramint.2019.03.020.

Zorba, V., Stratakis, E., Barberoglou, M., Spanakis, E., Tzanetakis, P., Anastasiadis, S.H., and Fotakis, C. (2008). Biomimetic artificial surfaces quantitatively reproduce the water repellency of a Lotus leaf. Adv. Mater. 20, 4049–4054. https://doi.org/10.1002/adma.200800651.